Geochemical and geochronological signatures of granitoids from the Chaillu massif, Congo Craton: Insights into Mesoarchean crustal growth

Olivier Blein, Thomas Fullgraf, Maxime Padel, Jérémie Melleton, Matthieu Chevillard, Eric Gloaguen, Florent Boudzoumou, Florence Cagnard, Benjamin Le Bayon, Louis-Marie Djama, et al.

Precambrian Research 409 (2024) 107435

Contents lists available at ScienceDirect

Precambrian Research

journal homepage: www.elsevier.com/locate/precamres

50th Anniversary Invited Review

Geochemical and geochronological signatures of granitoids from the Chaillu massif, Congo Craton: Insights into Mesoarchean crustal growth

O. Blein [a,*], T. Fullgraf [a], M. Padel [a], J. Melleton [a], M. Chevillard [a], E. Gloaguen [a,b], F. Boudzoumou [c], F. Cagnard [a], B. Le Bayon [a], L.-M. Djama [d,1], Y. Callec [a]

[a] BRGM, ISTO, UMR 7327, 3 av. Claude Guillemin, BP 36009, 45060 Orléans Cédex, France
[b] CNRS/ISTO, UMR 7327, 1A rue de la Férollerie, 45071 Orléans Cédex, France
[c] Université Marien Ngouabi, Département de Géologie, BP 69, Brazzaville, People's Republic of Congo
[d] Direction générale des Mines et de la Géologie, Ministère des Mines, Brazzaville, People's Republic of Congo

ARTICLE INFO

Keywords:
Congo Craton
Mesoarchean
TTG
sanukitoids
potassic granites
U-Pb age

ABSTRACT

We present new geochemical and geochronological data for Mesoarchean to Neoarchean plutons of the Chaillu inlier of the Congo Craton that demonstrate an evolution of magma sources in relation with crustal growth. Four distinct plutonic suites were newly identified: (1) sodic low medium/high-pressure tonalite-trondhjemite-granodiorite, (2) Mg–K-rich monzogranite to monzodiorite (sanukitoids), (3) K-rich monzogranite–syenogranite, (4) K-rich granodiorite–monzogranite with medium/high-pressure TTG-like signatures. The TTGs are metaluminous to slightly peraluminous, silica-rich magmatic rocks ($SiO_2 > 67.5$ wt%) with high contents of Na_2O (3.5 $< Na_2O <$ 6.2 wt%), and low contents of ferromagnesian oxides, and K_2O contents ($K_2O < 2.6$ wt%). The sanukitoids (s.l.) are metaluminous to slightly peraluminous, with a large range of silica contents (53 $< SiO_2 <$ 69 wt%), high Mg# (42–74) and potassic with variable K_2O contents (1.2 $< K_2O <$ 5.0 wt%). The high-K granites are slightly peraluminous, with high silica contents ($SiO_2 > 67.7$ wt%), low amounts of ferromagnesian oxides, and a clear potassic signature, with K_2O contents (2.5 $< K_2O <$ 4.7 wt%), and K_2O/Na_2O ratios higher than 0.55. The zircon U–Pb dating results indicate that: i) TTGs emplaced between 3012 ± 16 Ma and 2840 ± 9 Ma; ii) sanukitoids between 2853 ± 14 Ma and 2832 ± 9 Ma; and iii) are K-rich biotite granites between 2893 ± 11 Ma and 2847 ± 16 Ma. Two main well-defined periods are identified: i) one of TTG-type magmatism between 3.02 and 2.92 Ga; and ii) one of sanukitoid-TTG-biotite granite-type association between 2.91 and 2.82 Ga. Such temporal evolution from TTG-domination through coexisting sanukitoids (s.l.) – TTGs – biotite granites during the late-Archean in the Congo Craton resembles other Archean cratons, such as the Dharwar, North China, Karelian, Superior Province, Pilbara, Kaapvaal, São Francisco and Amazonian.

1. Introduction

The Late Meso- to Neoarchean (ca. 3.00 to 2.50 Ga) records fundamental and systematic changes in the petrogenesis and composition of intermediate to felsic granitoids that occur diachronously in individual cratons worldwide (Laurent et al., 2014). Mesoarchean TTG suites were accompanied and replaced progressively by high-K granodiorite and biotite-rich granite, syn- to post-tectonic A-type granitoids, and high-Mg sanukitoids (Bleeker, 2003; Moyen et al., 2003; Jayananda et al., 2006; Laurent et al., 2014; Farina et al., 2015; Dall'Agnol et al., 2017). The latter are high-Mg dioritic to granodioritic rocks (Martin et al., 2009) with an affinity to TTGs with whom they share some features (e.g., Shirey and Hanson, 1984; Smithies and Champion, 2000; Heilimo et al., 2010; Dey et al., 2014, 2016; Jayananda et al.,2018).

The important secular change in plutonism was concomitant to the onset of modern-style plate tectonics allowing crustal recycling in subduction and continental collision settings (Sylvester, 1994; Keller and Schoene, 2012; Laurent et al., 2014; Moyen and Laurent, 2018). Bédard et al. (2013) suggested alternatively *peri*-continental subcretion-imbrication being more efficient for transport of crustal material into the shallow mantle. In modern convergent margins, relative dense oceanic lithosphere is commonly the active agent dragging the

* Corresponding author.
E-mail address: o.blein@brgm.fr (O. Blein).
[1] deceased on 16/05/2020.

https://doi.org/10.1016/j.precamres.2024.107435
Received 17 January 2024; Received in revised form 6 May 2024; Accepted 17 May 2024
Available online 29 May 2024

underriding plate into the mantle. In contrast, during the late Archean, the lower plate composed of a buoyant stagnant-lid oceanic lithosphere behaving passively during subcretion and finally being overridden by advancing continents (Bédard et al., 2013).

The Archean Congo-Kasai craton underlies a large part of central Africa extending from the Democratic Republic of the Congo (DRC) through Congo-Brazzaville (=Republic of the Congo) and Gabon to southern Cameroun (Toteu et al., 1987; Nédélec et al., 1990). The NW part of the craton is exposed in Congo-Brazzaville and Gabon. As in other cratons worldwide, two main magmatic phases, Mesoarchean TTG suites and Neoarchean alkaline to calc-alkaline potassic granitoids were described in Gabon (Prian et al., 1991; Bouton et al., 2009; Thieblemont et al., 2009).

Similar granitoids were recognised by the French Geological Survel (Bureau de Recherches Géologiques et Minières: BRGM) in Congo-Brazzaville through regional mapping at 1:200,000 scale from 2013 to 2016 covering the entire Archean basement in this country (Chevillard et al., 2017a, 2017b, 2017c; Fullgraf et al., 2017; Gloaguen et al., 2017a, 2017b; Issautier et al., 2017; Paquet et al., 2017). Here, we present the whole-rock geochemistry and geochronology of rocks from the Chaillu inlier in order to elucidate their petrogenesis and timing of emplacement, thus contributing to the reconstruction of the geodynamic evolution of the Congo Craton during the Archean.

2. Geological setting

The Precambrian basement of central Africa (SW Cameroon, Equatorial Guinea, Gabon, Congo-Brazzaville, and DRC) consists of the Archean Congo-Kasai craton overlain by Paleoproterozoic sediments deposited in Eburnean (2.2–2.0 Ga) foreland basins and Neoproterozoic sediments of the Niari basin (Caen-Vachette et al., 1988; Prian and Johan, 1989; Chevallier et al., 2002; Thomas et al., 2001; Thiéblemont et al., 2009). Towards the west, the Precambrian rocks were overprinted progressively by both Eburnean and Pan-African deformation and metamorphism (Caen-Vachette et al., 1988; Kessi, 1992; Thiéblemont et al., 2009).

Archean rocks at the NW margin of the Congo Craton are exposed in several inliers which are locally known as Chaillu, Ivindo, and Kelle-Mbomo blocks (Kessi, 1992; Gatsé Ebotehouna et al., 2021; Loemba et al., 2023). They comprise essentially three rock associations: (1)

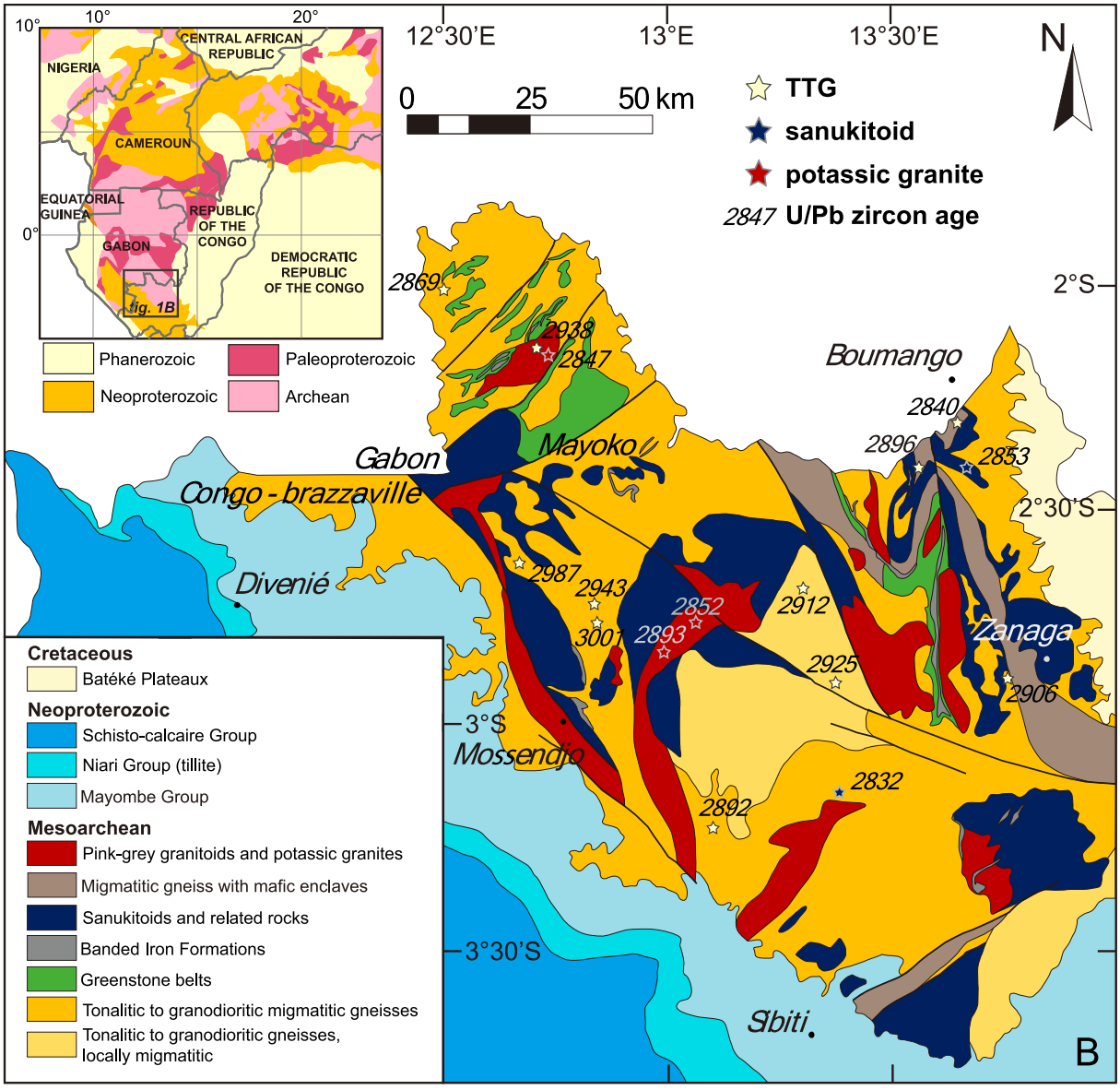

Fig. 1. Simplified geologic map of the NW part of the Congo-Kasai craton overlain by Paleoproterozoic foreland basins of the Eburnean orogeny and Neoproterozoic sediments of the Niari Basin (modified Thiéblemont et al., 2017).

Mesoarchean (2.93–2.87 Ga) grey tonalite-trondhjemite-granodiorite (TTG) orthogneisses; (2) greenstone belt slivers of mafic to ultramafic rocks with associated banded iron formations (BIF) classified as Belinga Group; and (3) Neoarchean (2.80–2.55 Ga) pink calc-alkaline to alkaline K-rich granitoids (Prian et al., 1991; Bouton et al., 2009; Thiéblemont et al., 2009). Neoarchean metamorphism (2.75 Ga) reached greenschist to amphibolite facies in the Belinga Group whereas the partly migmatitic orthogneisses record upper amphibolite to granulite facies conditions (Thiéblemont et al., 2009). Zircons from the metasedimentary rocks of the Belinga Group provided reliable and consistent ages between 2.92 and 2.87 Ga (Thiéblemont et al., 2009). They constitute maximum ages (inheritance) for the establishment of the Belinga Group. It can be concluded that the Belinga Group in the Chaillu inlier was deposited after 2.87 Ga and before 2.75 Ga.

The study area covers the southern half of the Chaillu inlier where basement rocks are commonly concealed below a thick horizon of regolith and weathered saprolith (Fig. 1). Rare outcrops are mostly limited to streams and rivers whereas BIF horizons and associated greenstones underlie elongated ridges standing out from the surrounding landscape.

Large areas of the Chaillu inlier are underlain by meso- to melanocratic grey orthogneisses of tonalitic to trondhjemitic composition; the igneous origin of these rocks is demonstrated by numerous amphibolite xenoliths of an older basement. The relatively homogeneous gneisses display commonly penetrative plane-parallel foliations defined by grain-flattening and oriented biotite. Local anatexis is recorded by intercalated, up to centimetre-wide, streaks and layers of granitic leucosomes, transposed into the regional gneissic fabric and consisting of K-feldspar, quartz, plagioclase and rare biotite. A second generation of weakly to undeformed, non-migmatitic tonalite and trondhjemite plutons has been emplaced into these gneisses after a first phase of regional metamorphism and deformation. The fine- to coarse-grained rocks comprise major amounts of plagioclase and quartz as major components, minor K-feldspar, biotite and amphibole as well as accessory apatite, epidote, zircon, and Fe-Ti oxides (Fig. 2).

The tonalitic and trondhjemitic rocks were intruded by large volumes of undeformed to moderately foliated, meso- to melanocratic, medium- to coarse-grained orthogneisses. The relative proportions of the main minerals K-feldspar, plagioclase, and quartz classify these rocks as quartz-monzodiorite, quartz-monzonite, and monzogranite (Fig. 2). Biotite and amphibole are minor components and the accessories Fe-Ti oxides, apatite, titanite, and zircon relatively abundant.

Fig. 2. Representative petrographic features of granitoids identified in the Chaillu inlier. (a) Strongly foliated tonalitic gneiss; (b-c) Photomicrograph of tonalite MO1151; (d) Deformed qtz monzonite; (e-f) Photomicrograph of qtz-monzonite MO1139; (g) Syenogranite MO1152: (h-i) Photomicrograph of syenogranite MO1152.

In the Chaillu massif, supracrustal rocks of the Belinga Group form elongated and polyphasely-deformed slivers, up to several kilometers long, or enclaves within magmatic rocks. Their spatial arrangement shows that they probably formed a single major horizon. The main outcrops of the Belinga Group are the greenstone belts of Mayoko and Zanaga. The Belinga Group is composed of four main lithologies: i) amphibolites; ii) banded iron formations; iii) pyroxenites; and iv) micaschists and paragneisses.

In the field, the amphibolites forms a succession of discontinuous enclaves, from a few hundred to several kilometers wide, in gneissic or granitic host-rocks. The migmatitic gneisses associated to BIF horizons are made of quartz, biotite, muscovite, garnet, tourmaline, and staurolite, and suggest that peak metamorphic conditions reached amphibolite to granulite facies. This metamorphic event is described as a charnockitic event at ca. 2.8–2.85 Ga (Mayaga-Mikolo, 1996; Thieblemont et al., 2009). Locally, discontinuous, up to several meter thick layers of ultramafic metapyroxenite and intercalated into mafic successions. Hornblende and plagioclase are the predominant minerals in the fine- to coarse-grained amphibolites, associated with biotite, and locally staurolite and/or garnet. Locally, metric layers of pyroxenites occur within amphibolites. In the Mayoko and Zanaga area, BIF consists of a millimetric to centimetric alternation of quartz-rich and iron oxide-rich layers.

In the Mayoko area, BIFs occurs as pluri-kilometric layers of several hundred of a meter thick. These layers correspond to the overturned flanks of a pluri-kilometric synclinal. The center of the syncline is composed of chlorite-schists, biotite-garnet paragneisses, and amphibolites.

In the Zanaga area, BIFs occur as pluri-kilometric lenses of several hundred of meters thick which correspond to ridge crests. The Zanaga BIFs show structures resulting from complex folding, faulting, and shearing. The predominant feature is an east steeply dipping N-S foliation. On a macroscopic scale, BIFs are affected by two successive folding stages. Outside of the BIF-rich zone, the Belinga Group is mainly composed of amphibolites and amphibolitic gneisses.

All igneous phases described before were intruded by a younger generation of plutons with up to several km-size, which are made of weakly to undeformed pink-grey monzogranite, granodiorite, and potassic granite.

Elongated bodies consist of coarse- to very coarse-grained rocks in their core, which towards the margin become finer-grained. High proportions of plagioclase (25–30 %) relative to K-feldspar (20–25 %; up to several cm size) and quartz (20–25 %) classify the first group of these late intrusions as monzogranite and granodiorite. Biotite (5–10 %) and amphibole (5 %) are minor components and the accessory phases Fe-Ti oxides, apatite, titanite, and zircon relatively abundant.

The second group consists of potassic granites that can be further subdivided into grey-pink biotite-rich and pink K-feldspar-rich, biotite-poor varieties (Fig. 2). Grey-pink, biotite-rich granites are homogeneous, with K-feldspars up to several cm-size set in an equigranular, coarse-grained quartz-feldspar matrix. The relative proportions of K-feldspar (20–25 %), quartz (25–30 %), plagioclase (15–25 %) classify these rocks as monzogranite. Biotite is the only mafic mineral and a major component (15–20 %); accessory minerals include zircon, magnetite, and apatite, the latter being sometimes enriched. Pink K-feldspar-rich granites display similar textures as the grey-pink variety. The modal proportions of K-feldspar (30–35 %), quartz (25–30 %), plagioclase (15–25 %) classify the rocks as monzogranite and syenogranite. In contrast to the first variety, biotite forms a minor component (<5%). The accessory minerals comprises again zircon, magnetite, and apatite.

3. Analytical methods

3.1. Whole-rock geochemistry

Whole-rock major and trace element compositions were determined at the ALS Minerals, Dublin, Ireland. For major elements, 0.9 g of ignited sample was added to 9.0 g of lithium borate flux (50 % $Li_2B_4O_7$, 50 % $LiBO_2$), mixed well, and fused at 1050–1100 °C. A flat, molten glass disc was prepared from the resulting melt, and analyzed by X-ray fluorescence spectrometry. For trace elements, 0.2 g of sample was added to 0.9 g of lithium metaborate flux, mixed well, and fused at 1000 °C. The resulting melt was cooled and dissolved in 100 mL of 4 % nitric acid, and the resulting solution was analyzed by ICP–MS.

3.2. U-pb zircon geochronology

Zircon was separated from fresh samples with rock grinding using a steel crusher. Grains were separated from the resulting powders using a heavy liquid, then using a magnetic separator. The selected grains were obtained from random handpicking under a binocular microscope and finally set in an epoxy resin puck and polished to expose their core. To identify internal growth textures and morphologies, zircon grains were imaged by scanning electron microscopy (SEM) to get cathodoluminescence and back-scattered electron images. The U-Pb age of zircon was determined in situ at the BRGM laboratory, Orléans, France, using LA-ICP-MS with a quadrupole ICP-MS X series II coupled to a Cetac Excite 193 nm laser with Ablation spot at 35 μm and energy pulses of 7 J·cm–2, and repetition rates of 8 Hz. The resulting ablated material was mixed in a He and Ar gas mixture before being transferred into the plasma source of the ICP-MS device. Analyses were standardized with zircon 91,500 (Wiedenbeck et al., 1995) and controlled with the Plešovice standard (338 ± 1 Ma, Sláma et al., 2008). Data reduction was done with GLITTER® software developed by Macquarie Research Ltd., and Concordia ages and diagrams were produced using the Isoplot/Ex v.3 software package (Ludwig, 2003). For ages > 1 Ga, we reported the $^{207}Pb/^{206}Pb$ ages, and for ages < 1 Ga, we used the $^{206}Pb/^{238}U$ ages. The analyses out of the [90–110 %] concordance interval, calculated with 100 × ($^{207}Pb/^{235}U$ age)/($^{207}Pb/^{206}Pb$ age) for ages > 1 Ga (Meinhold et al., 2011) and 100 × ($^{206}Pb/^{238}U$ age)/($^{207}Pb/^{235}U$ age) for ages < 1 Ga, were not taken into account (Faure and Mensing, 2005; Talavera et al., 2012). The results are given in supplementary material (Table S5).

4. Geochemistry

The results of the whole rock analyses of one hundred and thirty-eight samples are given in supplementary material (Tables S1 to S4). They are subdivided into the four groups of magmatic rocks that have been recognized in the field.

4.1. Tonalitic to trondhjemitic grey gneisses

In the Q' vs ANOR diagram of Streckeisen and Le Maitre (1979), the TTG samples are classified as tonalite (65 %), tronhjemite (25 %), granodiorite (15 %) and quartz-diorite (10 %) (Fig. 3).

SiO_2 concentrations range between 60.1 and 75.6 wt% and most oxides are negatively correlated with SiO_2. Exceptions are K_2O and Na_2O, which do not define clear trends. Most samples have high SiO_2 (>67.5 wt%), Na_2O (3.65–6.17 wt% – mean of 4.76 wt%) and Al_2O_3 (12.95–19.56 wt% – mean of 15.63 wt%), whereas MgO (0.12–4.09 wt% – mean of 1.19 wt%) and ferro-magnesian oxides are low ($Fe_2O_3^{tot}$ + MgO + MnO + TiO_2 mean of 4.98 wt%).

A/CNK (molar Al_2O_3/[CaO + Na_2O + K_2O]) ratios between 0.77 and 1.14 define the metaluminous to slightly peraluminous character, whereas the FeO^t/[FeO^t + MgO]) vs. SiO_2 and MALI index diagram demonstrate magnesian and calcic to calc-alkaline affinities of most samples (Fig. 4).

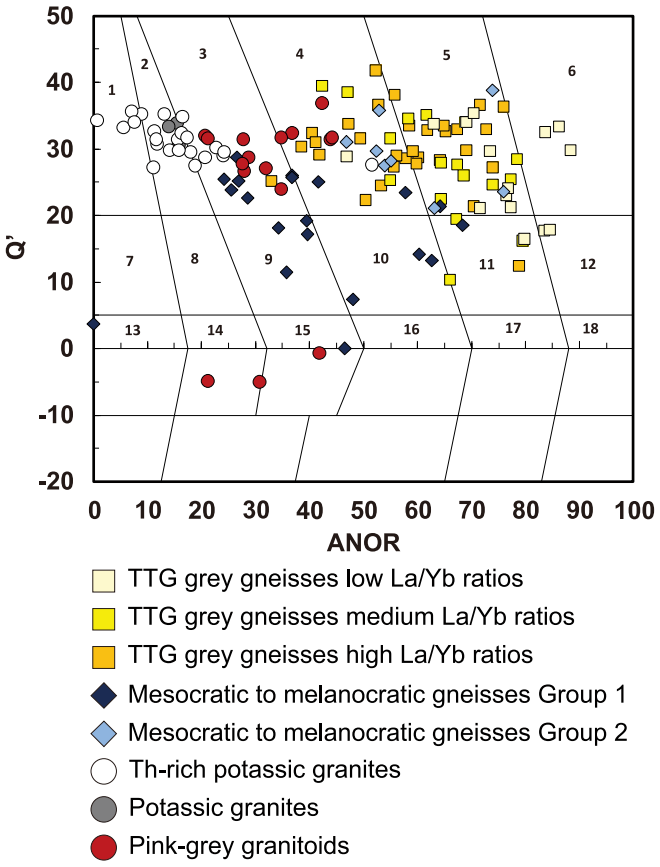

Fig. 3. Q' vs. ANOR normative composition classification diagram (Streckeisen and Le Maitre, 1979) for classification, where Q'=100*Q/(Q + Or + Ab + An) and ANOR = 100*An/(Or + An).

Na_2O/K_2O ratios between 1.52 and 11.05 and high Al_2O_3 concentrations (12.95–18.5 wt%) classify the rocks as high-Al TTG suite (Barker, 1979). The sodic character is characteristic for TTG suites (Martin, 1994).

Trace elements display low concentrations of compatible transition elements (Ni = 5–126 ppm, Cr = 10–130 ppm, and V = 9–134 ppm), relatively low HFSE (Nb = 1–17.8 ppm, Ta = 0.1–5.9 ppm, Zr = 54–235 ppm, Y = 2–25 ppm, and Hf = 1.8–7.0 ppm), and variable LILE contents, with low Rb (6–109 ppm) and moderately high Sr (133–1035 ppm) and Ba (101–1195 ppm).

REE patterns show general LREE enrichment but variable HREE depletion such that three subgroups with high (20–100; mean = 58; Fig. 5), medium (11–58; mean = 24; Fig. 5), and low (5–19; mean = 10; Fig. 5) $(La/Yb)_n$ ratios can be distinguished, which correlate well with decreasing Sr/Y ratios and increasing $(Yb)_N$ values (Fig. 6). However, all subgroups display similar Eu/Eu* anomalies between 0.7 and 1.3.

High- and medium $[La/Yb]_n$ rocks tend to be more peraluminous than those of lower $[La/Yb]_n$ ratios. The high $[La/Yb]_n$ subgroup includes most of the rocks classified as granodiorite and is the dominant group for tonalite and trondhjemite; ($Fe_2O_3^t$ + MgO + MnO + TiO_2) values are lower than 6 wt% (mean of 3.8 wt%). The medium $(La/Yb)_N$ subgroup comprises mostly tonalite, and few samples of trondhjemite and quartz diorite; ($Fe_2O_3^t$ + MgO + MnO + TiO_2) values vary from 2.3 to 9.9 wt% (mean of 5.1 wt%). The low $[La/Yb]_n$ subgroup includes again mainly tonalite, whereas trondhjemite and quartz diorite are rare; ($Fe_2O_3^t$ + MgO + MnO + TiO_2) values are higher than 5 wt% (mean of 7.3 wt%).

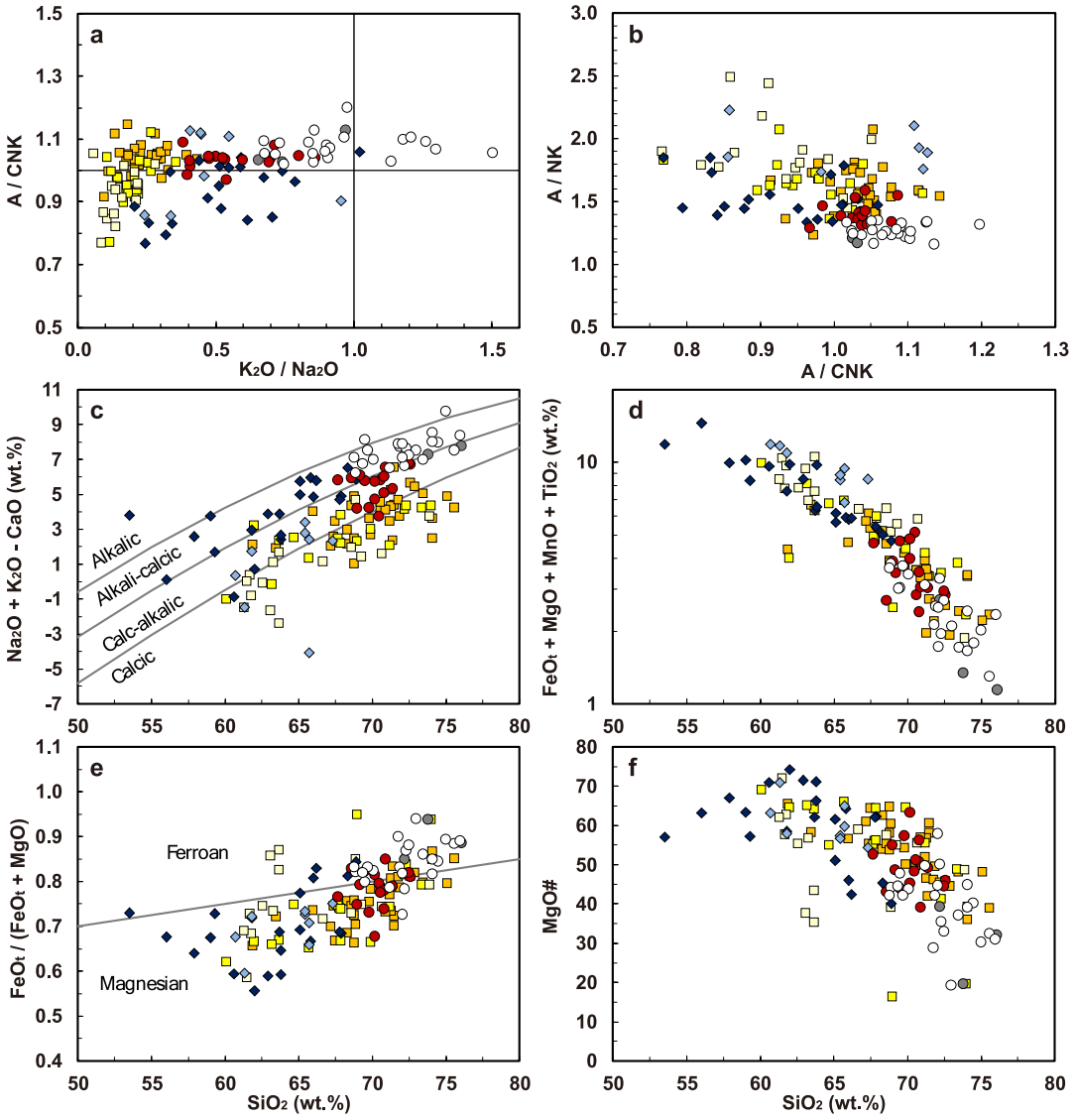

Fig. 4. Major-elements whole-rock geochemistry of plutonic rocks from the Chaillu inlier. a) A/CNK (molar $Al_2O_3/[CaO + Na_2O + K_2O]$ ratio) vs. K_2O/Na_2O ratios; b) A/NK vs A/CNK; c) MALI index ($[Na_2O + K_2O]$-CaO) vs. SiO_2 diagram of Frost et al. (2001); d) some of "mafic" oxides ($FeO^t + MgO + MnO + TiO_2$) vs. SiO_2; e) ($FeO^t/[FeO^t + MgO]$) vs. SiO_2, (the line separating ferroan from magnesian fields after Frost et al., 2001); and f) MgO vs. SiO_2. Symbols as in Fig. 5.

4.2. *Mesocratic to melanocratic gneisses*

Major and trace elements discriminate two groups of mesocratic to melanocratic gneisses.

The first group (G1) comprises gneisses with SiO_2 concentrations from 53.5 to 68.9 wt%. In the Q' vs ANOR diagram the samples plot in the qtz-monzodiorite, qtz-monzonite, and monzogranite fields (Fig. 3; Streckeisen and Le Maitre, 1979).

Except for TiO_2, K_2O, and Na_2O, the major elements are correlated negatively with SiO_2. In comparison with the TTG suite, the samples display generally lower Al_2O_3 (13.00–18.30 wt% – mean of 15.52 wt%), CaO (1.80–7.30 wt% – mean of 3.79 wt%), and Na_2O (3.23–7.03 wt% – mean of 4.32 wt%), and higher MgO (0.66–4.26 wt% – mean of 2.24 wt %) and K_2O (1.53–5.00 wt% – mean of 3.14 wt%) contents.

Further classification diagrams indicate the ferroan to magnesian, calc-alkaline to alkaline, metaluminous character of the rocks (Fig. 4). A/CNK ratios range from 0.77 to 1.04 (mean = 0.91) and K_2O/Na_2O ratios from 0.3 to 1.5 (mean = 0.77). $FeO^t/(FeO^t + MgO)$ ratios are relatively low (normally < 0.84) and show a positive correlation with silica (Fig. 4). The sum of ferro-magnesian oxides is high when compared to the TTG suite (4.7–14.5 wt% – mean of 7.77 wt%).

Trace elements are marked by high Ba (478–3310 ppm; mean of 1218 ppm) and Sr (275–1350 ppm; mean of 578 ppm) concentrations, and the samples have also high contents in transition elements such as V (31–180 ppm; mean of 87 ppm), Ni (8–116 ppm; mean of 40 ppm) and Cr (10–170 ppm; mean of 65 ppm). These rocks have low to moderate contents in HFSE (Zr = 95–565 ppm, generally < 350 ppm; Hf = 2.6–12.1 ppm; Y = 7.7–45.7 ppm; Nb = 4–36 ppm; Ta = 0.1–18.5 ppm). They show a wide range of $[La/Yb]_n$ ratios (15–125; Figs. 5-6), but most often higher than 30, with a discrete to moderate negative Eu anomaly (Eu/Eu* between 0.64 and 0.95), and low to moderate Sr/Y ratios (11–75; mean of 42).

The second group (G2) comprises gneisses with SiO_2 concentrations from 60.7 and 67.3 wt%. In the Q' vs ANOR diagram the samples plot in the granodiorite and tonalite (Fig. 3; Streckeisen and Le Maitre, 1979).

Except for TiO_2, K_2O, and Na_2O, the major elements are correlated negatively with SiO_2. In comparison with the TTG suite, the samples display generally lower Al_2O_3 (14.90–16.30 wt% – mean of 15.50 wt%), CaO (2.70–7.24 wt% – mean of 4.38 wt%), and Na_2O (1.30–3.75 wt% – mean of 3.21 wt%), and higher MgO (1.84–4.41 wt% – mean of 2.73 wt %), Fe_2O_3 (4.95–8.23 wt% – mean of 6.83 wt%) and K_2O (1.26–2.49 wt % – mean of 2.12 wt%) contents.

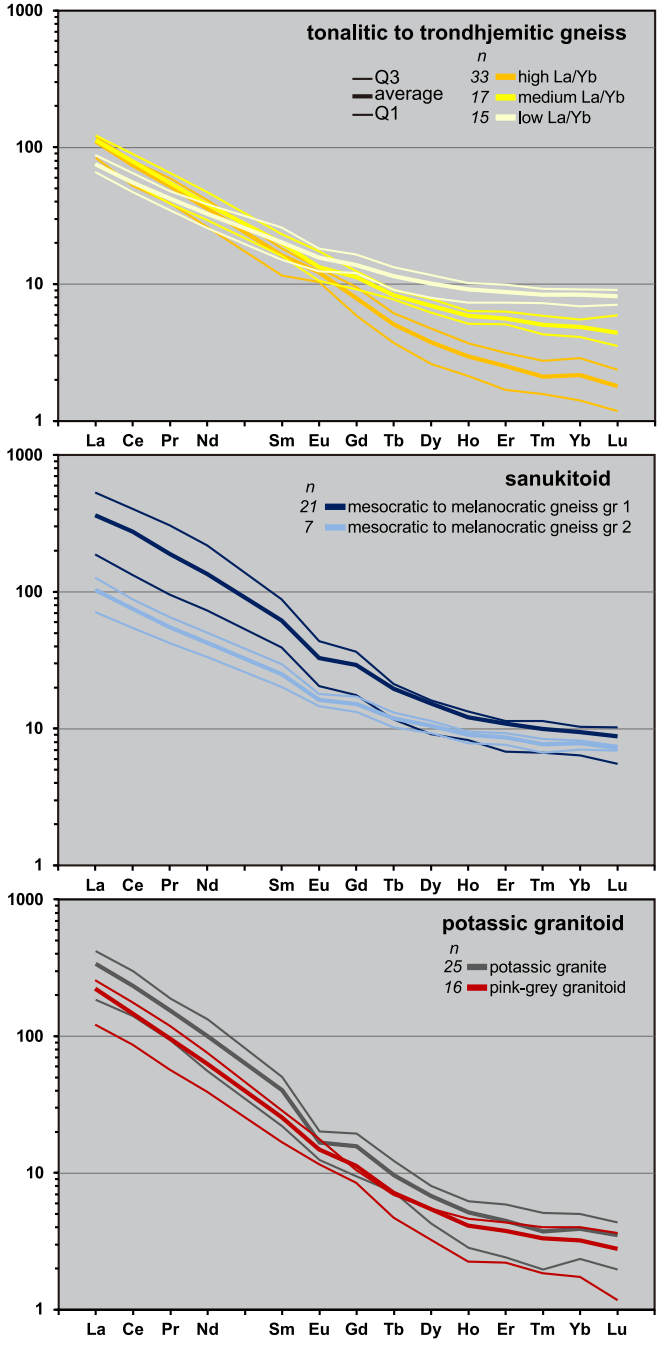

Fig. 5. Chondrite normalized diagram of the tonalitic to trondhjemitic grey gneisses, sanukitoids, and potassic granitoids. Normalization from Sun and McDonough, 1989.

Further classification diagrams indicate the magnesian, calcic to calc-alkaline, metaluminous to slightly peraluminous character of the rocks (Fig. 4). A/CNK ratios range from 0.86 to 1.13 (mean = 1.01) and K_2O/Na_2O ratios from 0.7 to 2.7 (mean = 0.73). $FeO^t/(FeO^t + MgO)$ ratios are relatively low (normally < 0.75) and show a positive correlation with silica (Fig. 4). The sum of ferro-magnesian oxides is high when compared to the TTG suite (6.8–11.9 wt% – mean of 9.59 wt%).

Trace elements are marked by moderate Ba (273–684 ppm; mean of 541 ppm) and Sr (173–404 ppm; mean of 312 ppm) concentrations. They have high contents in transition elements such as V (73–148 ppm; mean of 105 ppm), Ni (34–116 ppm; mean of 68 ppm), and Cr (60–170 ppm; mean of 110 ppm). These granitoids are depleted in HFSE (Zr = 100–358 ppm, generally < 200 ppm; Hf = 2.7–9.7 ppm; Y = 3.1–17.8

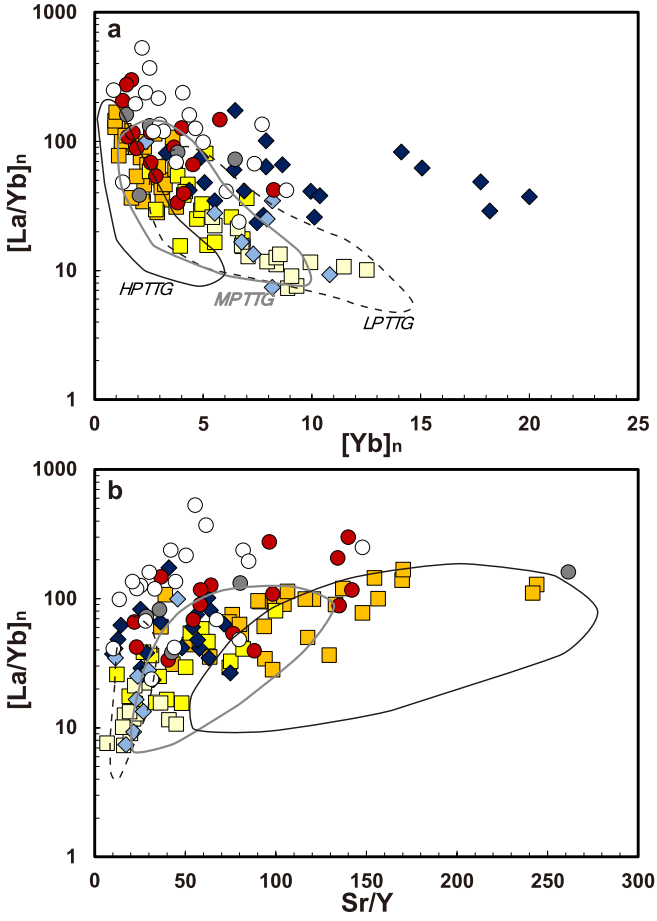

Fig. 6. A. $(La/Yb)_n$ vs. $(Yb)_n$ diagram. B. $(La/Yb)_n$ vs. Sr/Y diagram (LP, MP, HP TTG fields after Moyen, 2011). Symbols as in Fig. 5.

ppm; Nb = 2.0–7.1 ppm; Ta = 0.2–5.8 ppm). They are characterized by low $[La/Yb]_n$ (5–71; mean of 21; Fig. 6) with flat HREE patterns, and low to moderate Sr/Y ratios (11–46; mean of 25).

4.3. Potassic granites

Potassic granites comprises rocks with SiO_2 concentrations from 68.8 to 76.1 wt%. In the Q' vs ANOR diagram the samples plot in the monzogranite, syenogranite and alkaline granite fields (Fig. 3; Streckeisen and Le Maitre, 1979).

Except for TiO_2 and K_2O, the major elements are correlated negatively with SiO_2. In comparison with the TTG suite, the samples display generally lower Al_2O_3 (13.05–15.15 wt% – mean of 14.24 wt%), CaO (0.56–1.81 wt% – mean of 1.07 wt%), Na_2O (1.97–4.30 wt% – mean of 3.52 wt%), Fe_2O_3 (1.02–3.04 wt% – mean of 2.06 wt%), and MgO (0.08–0.65 wt% – mean of 0.35 wt%), and higher K_2O (4.26–7.86 wt% – mean of 5.08 wt%) contents.

Further classification diagrams indicate the ferroan to magnesian, calc-alkaline to alkali-calcic, slightly peraluminous to peraluminous character of the rocks (Fig. 4). A/CNK ratios range from 1.02 to 1.20 (mean = 1.08) and K_2O/Na_2O ratios from 0.99 to 3.99 (mean = 1.52). $FeO^t/(FeO^t + MgO)$ ratios are relatively low (normally < 0.90) and show a positive correlation with silica (Fig. 4). The sum of ferro-magnesian oxides is low when compared to the TTG suite (1.1–3.8 wt% – mean of 2.4 wt%).

Trace elements are marked by variable but generally high Ba (603–5450 ppm; mean of 1700 ppm) and Sr (99–591 ppm; mean of 331 ppm) concentrations, and low to moderate Rb (86–269 ppm; mean of 168 ppm) concentrations. The samples have also low contents in

transition elements such as V (6–32 ppm; mean of 18 ppm), Ni (5–48 ppm; mean of 9 ppm) and Cr (10–80 ppm; mean of 20 ppm). These rocks have low contents in HFSE (Zr = 33–433 ppm, generally < 300 ppm; Hf = 1.7–10.5 ppm; Y = 1.6–21.3 ppm; Nb = 0.8–12.7 ppm; Ta = 0.1–1.7 ppm). They show a wide range of $[La/Yb]_n$ ratios (17–380; Fig. 5), but most often higher than 40, with light negative Eu anomaly, and variable Sr/Y ratios (14–262; mean of 57). Th contents allow us to define two distinct groups, one group with Th contents between 8 and 16 ppm, and another group with Th contents between 23 and 80 ppm. Th-rich granites are characterized by higher contents in LREE ($45 < [La]_n < 827$; mean of 368), than Th-poor granites ($57 < [La]_n < 337$; mean of 188).

4.4. Pink-grey granitoids

Pink-grey granitoids comprises rocks with SiO_2 concentrations from 67.7 to 72.6 wt%. In the Q' vs ANOR diagram the samples plot in the granodiorite and monzogranite fields (Fig. 3; Streckeisen and Le Maitre, 1979).

Except for TiO_2 and K_2O, the major elements are correlated negatively with SiO_2. In comparison with the TTG suite, the samples display generally lower Al_2O_3 (13.80–16.30 wt% – mean of 14.73 wt%), CaO (1.40–2.56 wt% – mean of 2.06 wt%), Na_2O (3.52–4.75 wt% – mean of 4.11 wt%), Fe_2O_3 (1.81–4.08 wt% – mean of 2.83 wt%), and MgO (0.41–1.44 wt% – mean of 0.72 wt%), and higher K_2O (2.54–4.68 wt% – mean of 3.46 wt%) contents.

Further classification diagrams indicate the ferroan to magnesian, calc-alkaline to alkali-calcic, metaluminous to peraluminous character of the rocks (Fig. 4). A/CNK ratios range from 0.97 to 1.09 (mean = 1.03) and K_2O/Na_2O ratios from 0.58 to 1.31 (mean = 0.86). $FeO^t/(FeO^t + MgO)$ ratios are relatively low (normally < 0.82) and show a positive correlation with silica (Fig. 4). The sum of ferro-magnesian oxides is low when compared to the TTG suite (2.4–5.1 wt% – mean of 3.6 wt%).

Trace elements are marked by variable but generally high Ba (601–2230 ppm; mean of 1453 ppm) and Sr (246–696 ppm; mean of 444 ppm) concentrations, and low to moderate Rb (65–165 ppm; mean of 112 ppm) concentrations. The samples have also low contents in transition elements such as V (18–51 ppm; mean of 32 ppm), Ni (6–28 ppm; mean of 11 ppm) and Cr (10–80 ppm; mean of 26 ppm). These rocks have low contents in HFSE (Zr = 100–358 ppm, generally < 190 ppm; Hf = 2.7–9.7 ppm; Y = 3.1–14.7 ppm; Nb = 2.0–7.1 ppm; Ta = 0.1–5.8 ppm). They show a wide range of $[La/Yb]_n$ ratios (24–214; Fig. 5), but most often higher than 30, without negative Eu anomaly, and variable Sr/Y ratios (22–142; mean of 79).

Different components are involved in the genesis of pink-grey granitoids. They are typically intermediate in composition between TTGs, sanukitoids and potassic granites.

5. Geochronology

All analyzed samples are presented here in the Wetherill diagrams with lower and upper intercepts. Ages obtain for the most concordant populations, consistently equivalent within error or close to those obtained by the upper intercept, are interpreted as emplacement age. In this way, the ages of the lower intercepts are interpreted as a continuous diffusion process of radiogenic lead. The complete concordia diagrams for all the studied samples are in the supplementary material.

5.1. Tonalitic to trondhjemitic grey gneisses

5.1.1. Low La/Yb TTG suite

Sample MO4193 contains one homogeneous population of pink to brownish, mostly translucent long prismatic zircons with well-expressed or slightly blunted pyramids. They are microfissured and often contain inclusions. Some of them are composed of distinct inherited cores with rim overgrowths. Thirty analyses were made on 22 zircon grains. Analysis n°7 shows important common lead contamination, and was not further considered for age calculation. The remaining 29 data constrain upper and lower discordia intercept ages of 2932 ± 12 Ma and 594 ± 250 Ma, respectively. Most ages scatter between 2900 and 2970 Ma. In this interval, 5 analyses yielded a concordant age of **2943 ± 6 Ma** (MSWD = 2.8, n = 5), which is interpreted as time of zircon crystallization during magmatic emplacement (Fig. 7**A**).

Zircons from sample ZA8182 are mostly smaller than 100 μm, heterogeneous in shape and color, and translucent to red. 45 analyses were performed in the cores and rims of 36 zircons yielded two age groups. Age data from the cores record inherited ages of 2988 ± 17 Ma (MSWD = 1.5; Fig. 7**D**) and 3100 ± 28 Ma (MSWD = 0.49; Fig. 7**E**). Eleven out of the remaining 38 data yield a concordant age of **2925 ± 9 Ma** (MSWD = 1.3; Fig. 7**F**).

5.1.2. Medium La/Yb TTG suite

Zircon grains from sample MO1151-1 vary in size from tens to hundreds of μm forming one homogeneous population of pink to beige-pink, translucent, long prismatic crystals with commonly only few microcracks. 7 analyses yielded a concordant age of **2938 ± 10 Ma** (Fig. 7**B**) which is interpreted as time of zircon crystallization during magmatic emplacement.

Zircons from sample MO2289 are mostly larger than 200 μm forming one homogeneous population of blunt, pink to translucent long prismatic crystals. 30 analyses on 30 grains yield an upper intercept age of 2847 ± 29 Ma (MSWD = 0.12). Out of these, the seven most concordant data constrain the age of **2869 ± 14 Ma** (MSWD = 1.4, n = 7) (Fig. 7**C**).

Sample MO4163-2 contains many zircons forming a homogeneous population of very long prismatic, mostly pink to beige-pink zircons with blunt tips that often display microcracks and contain inclusions. Smaller grains are mostly translucent whereas larger grains are sometimes rather opaque. 16 out of 30 analyses on 30 grains yielded a concordant age of **3001 ± 9 Ma** (MSWD = 0.2, n = 16) (Fig. 7**G**).

Sample MO8068 contains a homogeneous population of translucent pink zircons that are sometimes fractured and containing often inclusions. 30 analyses were made on 23 crystals. Analysis 19 from the rim of a zircon plots above the Concordia and indicates a poorly defined age of 2873 Ma being younger than the average calculated from the other analyses. The significantly higher U concentration and U/Th ratio suggests the interpretation of metamorphic overgrowth. The remaining samples define upper and lower discordia intercept ages of 2968 ± 11 Ma, respectively (MSWD = 0.82). The six most concordant analyses yielded an age of **2987 ± 8 Ma** (MSWD = 0.15, n = 6 (Fig. 7**H**).

Zircons in sample ZA4265-1 vary in size from 30 μm to 300 μm, are mostly long prismatic with blunt tips, beige to smoky yellow–brown color and often microfractured. 30 analyses on 30 grains yielded upper intercept ages of 2977 ± 31 Ma (MSWD = 0.24). The six most concordant constrain the age of **3012 ± 16 Ma** (MSWD = 0.3, n = 6) (Fig. 7**I**).

5.1.3. High La/Yb TTG suite

Sample SB8197-2 contains very small long prismatic, colorless to slightly pink zircons, which are mostly milky. 30 analyses were performed on 26 grains. Out of these, 23 analyses yielded an upper Discordia age of 2864 ± 39 Ma (MSW = 0.65). The three most concordant analyses gave an age of **2892 ± 18 Ma** (MSWD = 0.93, n = 3; Fig. 7**J**).

Zircons from sample ZA6140-b vary from small pink translucent crystals through larger, pinkish-beige more or less translucent ones to large, relatively anhedral, opaque brown grains, which are sometimes metamict. 105 analyses were performed on 78 zircon grains to identify ages of possible inheritance. However, most of the analyses are highly discordant yielded an upper intercept age of 2867 ± 22 Ma. The five most concordant data yielded an age of **2896 ± 7 Ma** (MSWD = 1.6, n = 5) (Fig. 7**K**).

Zircons from sample ZA6195 are beige to brownish in color, long prismatic, and larger than 100 μm. 105 analyses were performed on 105

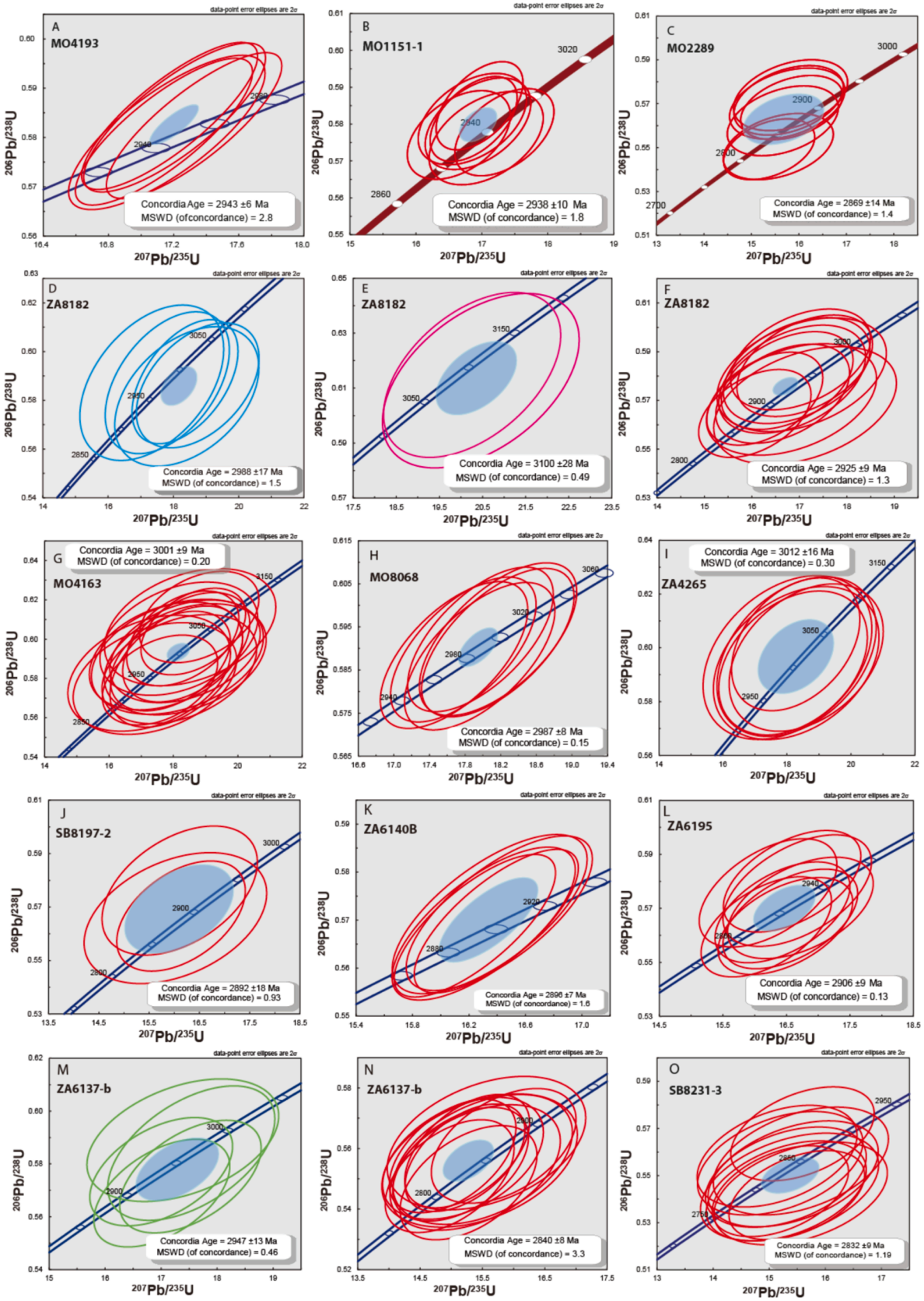

Fig. 7. A. Wetherill diagram for sample MO4193, Concordia age obtain on 5 analyses giving an age of **2943 ± 6 Ma**. **B.** Wetherill diagram for sample MO1151-1, Concordant age obtain from 7 analyses giving an age of **2938 ± 10 Ma**. **C.** Wetherill diagram for sample MO2289, Concordant age obtain from 7 of the most concordant analyses giving an age of **2869 ± 14 Ma**. **D-E.** Wetherill diagram for core analyses of sample ZA8182; two concordant ages can be calculated at **2988 ± 17 Ma** (**D**) and **3100 ± 28 Ma** (**E**). **F.** Wetherill diagram for Rim analyses of sample ZA8182; a concordant age can be calculated at **2925 ± 9 Ma**. **G.** Wetherill diagram for sample MO4163-2, Concordant age obtain from 16 analyses giving an age at **3001 ± 9 Ma**. **H.** Wetherill diagram for sample MO8068, Concordant age

obtains from 6 analyses giving an age at **2987 ± 8 Ma**. **I.** Wetherill diagram for sample ZA4265-1, Concordant age obtains from 6 analyses giving an age at **3012 ± 16 Ma**. **J.** Wetherill diagram for sample SB8197-2, Concordia age obtain from 3 analyses giving an age at **2892 ± 18 Ma**. **K.** Wetherill diagram for sample ZA6140B, Concordia age obtain from 5 analyses giving an age at **2896 ± 7 Ma**. **l.** Wetherill diagram for sample ZA6195, Concordia age obtain from 19 analyses giving an age at **2906 ± 9 Ma**. **M.** Wetherill diagram for sample ZA6137-b, Concordia age obtained from the 5 oldest analyses from core analyses giving an inherited age at 2947 ± 13 Ma. **N.** Wetherill diagram for sample ZA6137-b, analyses carried out on the rim give a Concordia age of **2840 ± 8 Ma**. **O.** Wetherill diagram for sample SB8231-3, Concordant age obtain from 11 rim analyses of sample SB8231-3 giving an age of **2832 ± 9 Ma**. ***P.*** *Concordant age obtain from 3 core analyses of Sample SB8231-3 giving an inherited age at 2960 ± 18 Ma.* ***Q.*** *Wetherill diagram for sample ZA6142, Concordia age obtain from 5 rim analyses of sample ZA6142 giving an age of* ***2853 ± 14 Ma.*** ***R.*** *Wetherill diagram for sample MO1152, Concordia age obtain for sample MO1152 based on the 4 most concordant analyses, giving an age at* ***2847 ± 16 Ma.*** ***S.*** *Wetherill diagram for sample ZA4184, Concordia age obtain from 8 analyses of sample ZA4184 giving an age of* ***2893 ± 11 Ma.*** ***T.*** *Wetherill diagram for sample ZA4187, Concordia age obtain from 5 analyses of sample ZA4187 giving an age of* ***2852 ± 13 Ma***

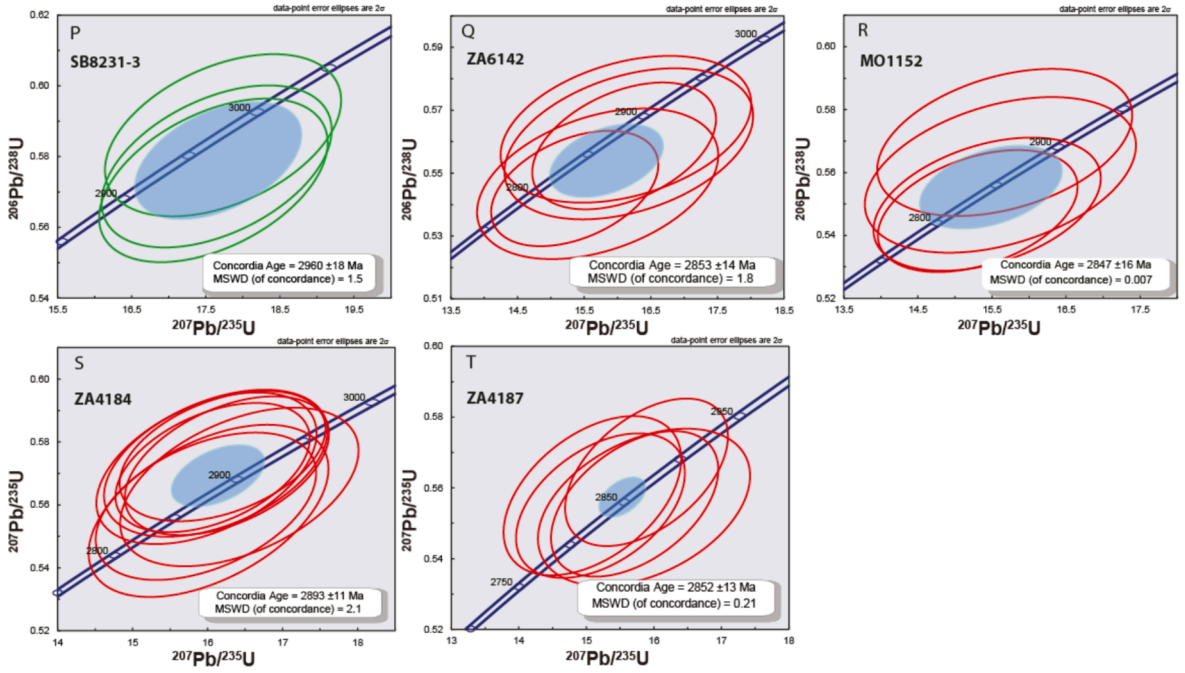

Fig. 7. (*continued*).

grains. Five analyses show significant common lead concentrations and were not further considered. The remaining data are again highly discordant or even inverse yielded upper ages of 2919 ± 11 Ma. The 19 most concordant data constrain the age at **2906 ± 9 Ma** (MSWD = 0.41, n = 8 (Fig. 7**L**).

Zircons from sample ZA6137-b are often larger than 200 μm, long prismatic, blunt, and pink to translucent. About 120 zircons were extracted and 30 analyses were performed. The zircons display under cathodoluminescence zonation characterized by very bright cores and darker rims corresponding to two age groups. Analyses in the cores yielded an upper discordia intercept age of 2952 ± 49 Ma. From these core analysis, 5 have yielded a concordant age of 2947 ± 13 Ma (MSWD = 0.46, n = 5; Fig. 7**M**) suggesting an assimilation of crustal host rock into the magma and interpreted as inherited age. Other analysis from the rim constrained a concordia age of **2840 ± 8 Ma** (MSW = 3.3, n = 12; Fig. 7**N**) considered as timing of zircon crystallization during magmatic emplacement.

5.2. Mesocratic to melanocratic gneisses

Zircons from sample SB8231-3 are mostly larger than > 200 μm, short prismatic, blunt, and microfractured. They vary in colors from light beige, pinkish red to dark brown. Thirty analyses from the cores and rims of eleven zircon grains yielded significantly different concordant ages of **2832 ± 9 Ma** (rim, Fig. 7**O**) and 2960 ± 18 Ma (core, Fig. 7**P**), which are interpreted to record the timing of zircon crystallization during magmatic emplacement and assimilation of an older crustal component.

Zircons from sample ZA6142 are generally less than 80 μm in size, long prismatic, blunt, and beige to translucent. Thirty-one analyses yielded an upper intercept age of 2899 ± 27 Ma (MSWD = 1.7). The five most concordant analyses define a concordant age of **2853 ± 14 Ma** (MSWD = 1.8, n = 5; Fig. 7**Q**).

5.3. Potassic granites

Zircons of sample MO1152 are smaller than 100 μm, long prismatic, and mostly very metamict displaying white to dark orange and sometimes pink colors. Thirty analyses were performed yielded an upper intercept age of 2849 ± 58 Ma. The four most concordant analyses constrain the age of **2847 ± 16 Ma** (MSWD = 0.007, n = 4, Fig. 7**R**).

Zircons from sample ZA4184 are mostly smaller than 50 μm, anhedral (rounded) to subhedral, and pink in color except for few orange or colorless grains. Most of the crystals are metamict. Eight out of thirty analyses yielded a concordia age of **2893 ± 11 Ma** (MSWD = 2.1, n = 8, Fig. 7**S**).

Zircons from sample ZA4187 are larger than 100 μm, long prismatic and slightly blunt. Pale beige to colorless, milky appearance reflects strong metamictization. 16 out of 30 analyses yielded an upper intercept age of 2865 ± 44 Ma (MSWD = 0.41). The most concordant analyses (red circle Fig. 7**T**) constrained an age of **2852 ± 13 Ma** (MSWD = 0.21, n = 5).

6. Discussion

6.1. Petrogenesis of plutonic rocks

The igneous suites of the Chaillu inlier show typical characteristics of

Meso to Neoarchean granitoids worldwide, such as the predominance of Na-rich plutonic rocks, the presence of sanukitoids and potassic granitoids, as well as general increase of K_2O with decreasing age (e.g., Laurent et al., 2014). Petrography, geochemical composition and U-Pb geochronology demonstrate systematic change in magma sources, the depth of melting, and the amount of assimilated crust with time. Petrography and geochemical composition reveals four major classes of TTG, mesocratic orthogneiss, potassic granite and pink-grey granitoids.

6.1.1. *Tonalitic to trondhjemitic grey gneisses*

The binary geochemical diagrams of Figs. 6 and 8 discriminate different TTG types and potassic magmas (Moyen, 2011). The increase in the $[La/Yb]_n$ ratio is attributed to residual garnet at greater depths fractionating Y and HREE during anatexis from the LREE released into the ascending magma. In contrast, plagioclase (Sr, Eu) is stable in higher crustal levels leading to negative Eu anomalies when the magma originates there (Halla et al., 2009; Moyen, 2011).

The TTGs of the Chaillu inlier have been classified into three groups (Figs. 6 and 8). The first group is marked by high Y (10–25 ppm), low Sr (<400 ppm), low Sr/Y ratios (<45) and weakly fractionated HREE profiles ($[La/Yb]_n < 20$; $[Gd/Er]_n < 2$). The samples of this group show affinity with low-pressure TTG suites (Moyen, 2011). The second group is characterized by intermediate Y (5.5–14.5 ppm), variable Sr (133–979 ppm), variable Sr/Y ratios (12–100), and weakly to clearly fractionated HREE profiles ($11 < [La/Yb]_n < 58$; $1.8 < [Gd/Er]_n < 3.5$). They can be associated with medium-pressure TTG suites. The third group combines samples with low Y (1.5–9.5 ppm), high Sr (>300 ppm), high Sr/Y ratios (generally > 60), and fractionated HREE profiles ($20 < [La/Yb]_n < 120$; $[Gd/Er]_n > 2.2$) with Er concentrations below 0.6 ppm. They plot mostly in the fields of medium and high-pressure TTGs.

The geochemistry of low La/Yb TTG suites is consistent with derivation from plagioclase and garnet-amphibolite, without garnet in the residue (Halla et al., 2009; Moyen, 2011), which constrains maximum melting pressures to ca. 1.0 GPa (<30 km depth; Almeida et al., 2011; Johnson et al., 2013; Nagel et al., 2012). In contrast, medium La/Yb TTG melts originated in equilibrium with garnet-rich, plagioclase-poor amphibolite and rutile-bearing eclogite with residual garnet, respectively (Halla et al., 2009; Moyen, 2011). High La/Yb TTG melts result from melting of hydrous mafic rocks at pressures of 1.4 to 1.8 GPa (ca. 45–60 km depth; Nagel et al., 2012). Recently, Ge et al., (2018,2022) propose a new model involving water-flow melting of Archean oceanic arcs at different depths to explain the origin of the different types of TTG. In this model, low and medium-pressure Archean TTGs were produced by water-flow melting of thick proto-arcs built on thick oceanic crust, while high-pressure TTGs were formed by water-flow melting of subducted arcs during intermittent subduction and arc accretion (Ge et al., 2018, 2022).

6.1.2. *Mesocratic to melanocratic gneisses (sanukitoids)*

G1 group orthogneisses of quartz-monzodiorite, monzonite, and granite composition are LILE-rich (Ba + Sr > 1400 ppm, Ba > 500 ppm, Sr > 450 ppm, and Th > 6 ppm) with depletion in HFSE (Nb, Ta, Ti, and P). Relatively high Er contents (0.8–4.4 ppm) indicate the absence of residual garnet in their source and therefore origin from shallower depths. Their REE patterns are similar to those of medium La/Yb TTGs, however Yb, Y and Er concentrations are higher. Their affinity to calc-alkaline suites is reflected in increased K (1.5–5 wt%) and Nb (>5 ppm) contents and high Mg# (0.40–0.74). In general, mesocratic to

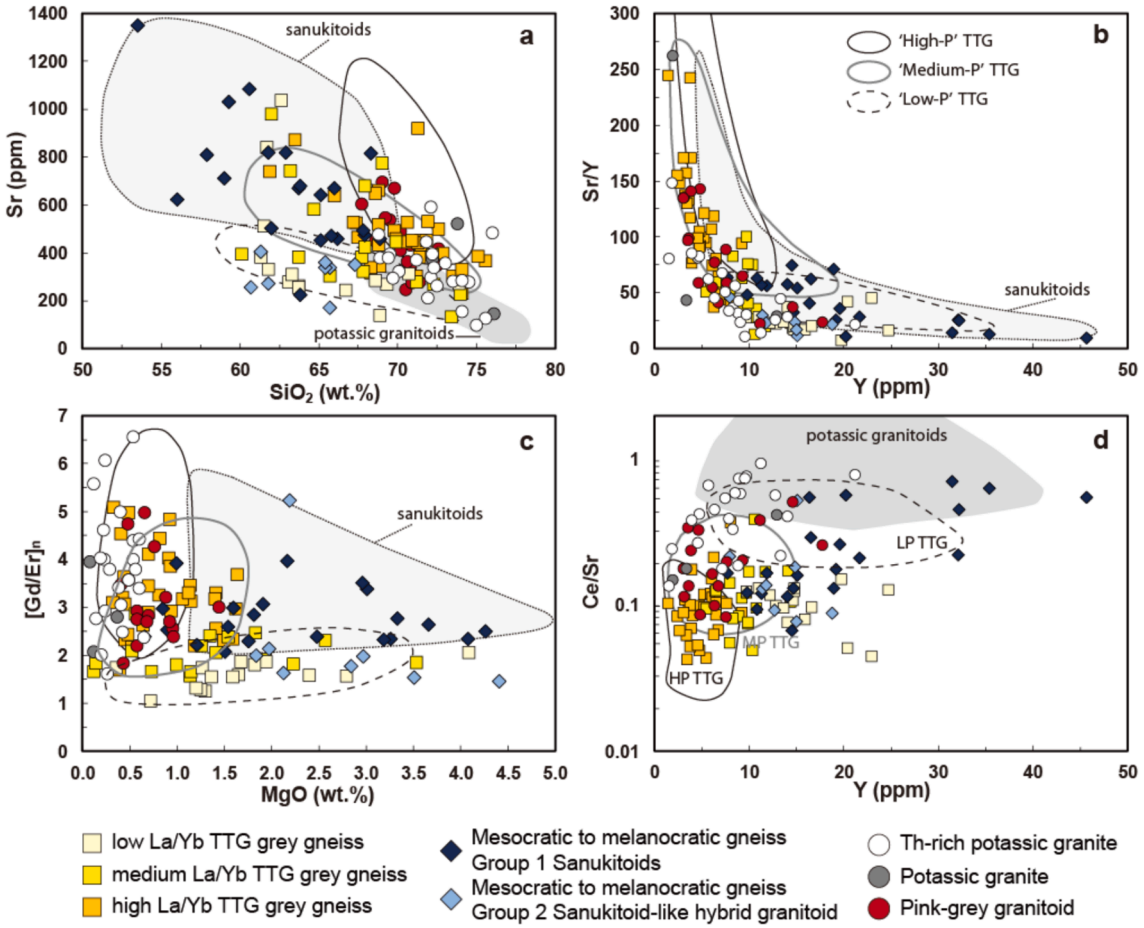

Fig. 8. Binary geochemical diagrams with fields of the three TTG groups, a potassic group of Moyen (2011), and sanukitoids of Halla et al. (2009): high-pressure TTG group (HP TTG); medium-pressure TTG group (MP TTG); low-pressure TTG group (LP TTG). (a) Sr vs. SiO_2, (b) Sr/Y vs. Y, (c) $(Gd/Er)_n$ vs. MgO, (d) Ce/Sr vs Y.

melanocratic gneisses with quartz-monzodioritic, monzonitic, and granitic compositions have akin to sanukitoids.

In comparison with high-pressure TTGs, sanukitoids are enriched in MgO (Fig. 8**A**), which may reflect the contribution of a mantle component to dioritoid and granitoid petrogenesis. However, in a diagram based on experimentally derived partial melts, sanukitoids straddle from amphibolite (as a major component) to greywacke source rocks (Fig. 9) suggesting involvement of crustal and/or mantle components in their genesis (Smithies and Champion, 2000). Such chemical features reflect interactions between mantle peridotite and a component rich in large-ion lithophile and high-field-strength elements (LILE, HFSE; Laurent et al., 2014). This component could be: i) a silicate melt, therefore the sanukitoids are the result of interaction between mantle wedge metasomatized and crustally-derived magmas (TTG melt) at lower crust (>1.2 GPa) conditions (Whalen et al., 2004; Halla et al., 2009; Heilimo et al., 2010; Almeida et al., 2010; Laurent et al., 2014); or ii) derived from sedimentary material, therefore the sanukitoids are the result of mantle wedge-sediment interaction (Halla, 2005; Laurent et al., 2011; Mikkola et al., 2011). The compositions of the quartz-monzodiorites to granites show a wide range of values for Ba + Sr and ΣLREEs. Few samples are characterized by ΣLREEs lower than 250 ppm with Ba + Sr values ranging from 1100 to 2100 ppm (Fig. 10). These samples share similarities with sanukitoids produced by interaction between peridotite and TTG. By contrast, others samples with ΣLREEs higher than 250 ppm and high Ba + Sr values (1000 – 4000 ppm) share similarities with sanukitoids produced by interaction between peridotite and sediments (Fig. 10). We therefore conclude that these rocks derive from two distinct interactions.

Orthogneisses with tonalitic and granodioritic composition (G2 group) show a small range in SiO_2 (60.7–67.3 wt%), with low MgO (1.8–4.4 wt%), and moderate K_2O (1.3–2.5 wt%) contents, and low K_2O/Na_2O (0.4–1.4) and $(Gd/Er)_n$ (1.5–5.2) ratios, as well as high Mg# (54–71) and (Ba + Sr) (735–1024 ppm) values (Fig. 8). The Yb and Y concentrations are moderate and REE patterns moderately fractionated.

Orthogneiss of tonalitic to granodioritic composition (G2 group) differs from the medium La/Yb TTG suites by higher MgO, Cr, and Ni content, and less fractionated REE pattern, but shows high affinity with the low La/Yb TTG suite. Compared to sanukitoids, the rocks have lower $(La/Yb)_n$ ratios and, at similar silica, lower NaO_2, K_2O, and Gd and higher $Fe_2O_3^t$, CaO, and MgO contents. This is taken as evidence of mingling and/or mixing between contrasting magmas, such as sanukitoid and TTG and the classification as hybrid granitoids with sanukitoid affinity.

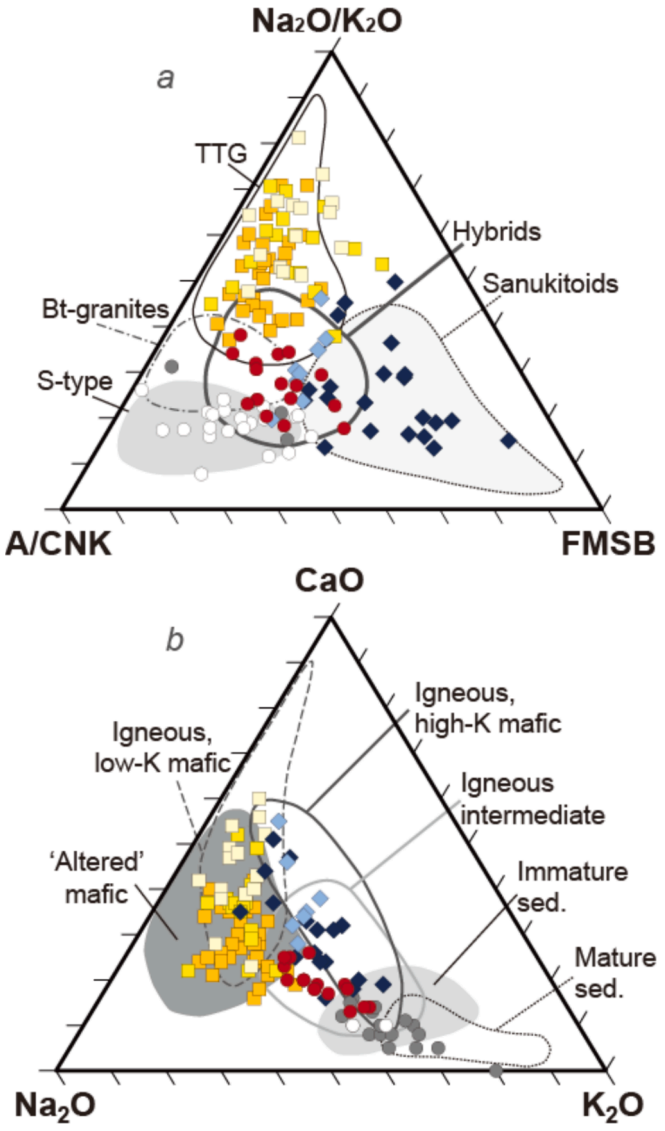

Fig. 9. A. Ternary a/cnk-na_2O/K_2O-FMSB ($[FeO^t + MgO]_{wt.\%}$*$[Sr + Ba]_{wt.\%}$) diagram (Laurent et al., 2014) where the compositions of the Chaillu granitoids are compared to those of the main types of Arhcean granitoids (Laurent et al., 2014) and Phanerozoic S-type granites (Laurent et al., 2017). B) Ternary Na_2O-CaO-K_2O diagram comparing the compositions of the Chaillu granitoids with those of experimentals melts derived from a range of starting materials produced at conditions relevant for crustal melting, including low-K igneous mafic rocks (Beard and Lofgren, 1991; Rapp and Watson, 1995; Wolf and Wyllie, 1994); "altered" (high-Na) igneous mafic rocks (Skjerlie and Johnston, 1996; Zamora, 2000); high-K igneous mafic rocks (Alonso-Perez et al., 2009; Almeev et al., 2013; Blatter et al., 2013; Sisson et al., 2005; Sisson and Grove, 1993); igneous intermediate rocks (Bogaerts et al., 2006; Martel et al., 1999; Singh and Johannes, 1996; Watkins et al., 2007); immature (greywacke) sediments (Montel and Vielzeuf, 1997; Patiño-Douce and Beard, 1996; Stevens, 1995; Vielzeuf and Holloway, 1988) and mature (pelitic) sediments (Patiño-Douce and Johnston, 1991; Patiño-Douce and Harris, 1998; Pickering and Johnston, 1998; Vielzeuf and Holloway, 1988).

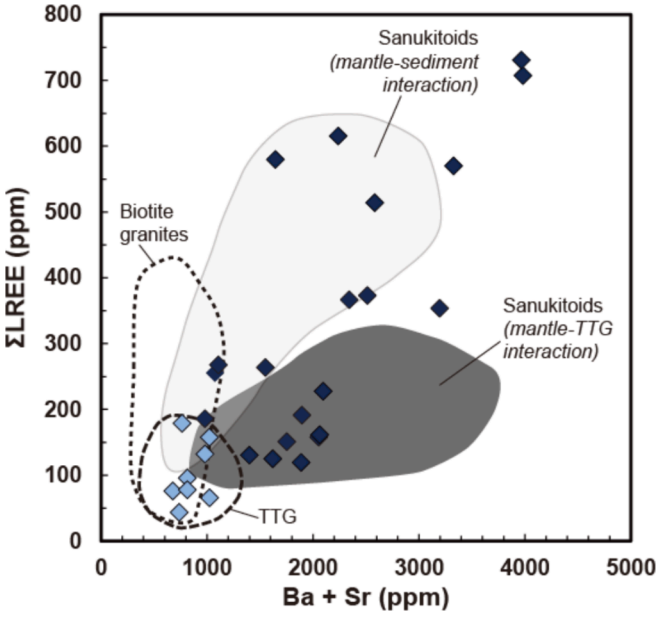

Fig. 10. ΣLREE (La + Ce + Pr + Nd) vs. Ba + Sr concentrations of mesocratic to melanocratic orthogneisses, compared with sanukitoids. Light gray field: Sanukitoids derived from interaction between mantle peridotite and paragneiss. Dark gray: Sanukitoids derived from interaction between mantle peridotite and TTG melts (Laurent et al., 2011, 2014).

6.1.3. Potassic granites

The geochemistry of potassic granites is defined by a narrow range in SiO_2 (68.8–76.1 wt%), MgO (0.08–0.60 wt%), K_2O (4.1–7.9 wt%) contents and high K_2O/Na_2O (1.0–4.0) and $(Gd/Er)_n$ (1.6–6.6) ratios, and the sum of (Ba + Sr) concentration generally above 1300 ppm (Fig. 8).

The granites display the highest fractionated REE patterns (Figs. 5-6). They differ from TTG and sanukitoid by lower MgO, Cr, and Ni contents. LREE contents are similar to sanukitoid, while HREE contents are commonly between TTG and sanukitoids. Altogether, the rocks show geochemical affinity with biotite granite (Moyen et al., 2003). All features demonstrate the different petrogenesis related to anatexis of TTG source rocks in the lower crust (>1.2 GPa) (Whalen et al., 2004; Almeida et al., 2010; Laurent et al., 2014).

6.1.4. Pink-grey granitoids

The geochemistry of pink-grey granitoids is defined by a narrow range in SiO_2 (67.7–72.6 wt%), MgO (0.41–1.44 wt%), K_2O (2.5–4.7 wt %) contents, moderate K_2O/Na_2O (0.6–1.3) and high $(Gd/Er)_n$ (1.8–5.0) ratios, and the sum of (Ba + Sr) concentrations above > 1500 ppm (Fig. 8).

These rocks display highly fractionated REE patterns, intermediate between potassic granite and high La/Yb TTGs (Fig. 8). The major-element composition indicates mixing of various sources resulting in a hybrid magma (Fig. 9; Laurent et al., 2014). This could be magma mixing of differentiated sanukitoid with a TTG (Almeida et al., 2010), assimilation of crust into TTG melts from the lower mafic crust (Jayananda et al., 2006; Smithies and Champion, 2000), mixing of TTG magma with enriched mantle (Prabhakar et al., 2009) or a complex interplay of these different mechanisms (Champion and Sheraton, 1997).

Pink-grey granitoids of the Chaillu inlier share with the TTG suites high $\Sigma(FeO^t + MgO + MnO + TiO_2)$, REE and HFSE concentrations, while the $CaO/(Na_2O + K_2O)$ and K_2O/Na_2O ratios, as well as Rb, Ba concentrations, are similar to those of biotite- and two-mica granite. This suggests interaction of felsic magma derived from the differentiation of TTG with crustal melts (similar in composition to biotite- and two-mica granites). The relative enrichment in Ba and Sr distinguishes the transitional gneisses from TTG and sanukitoid.

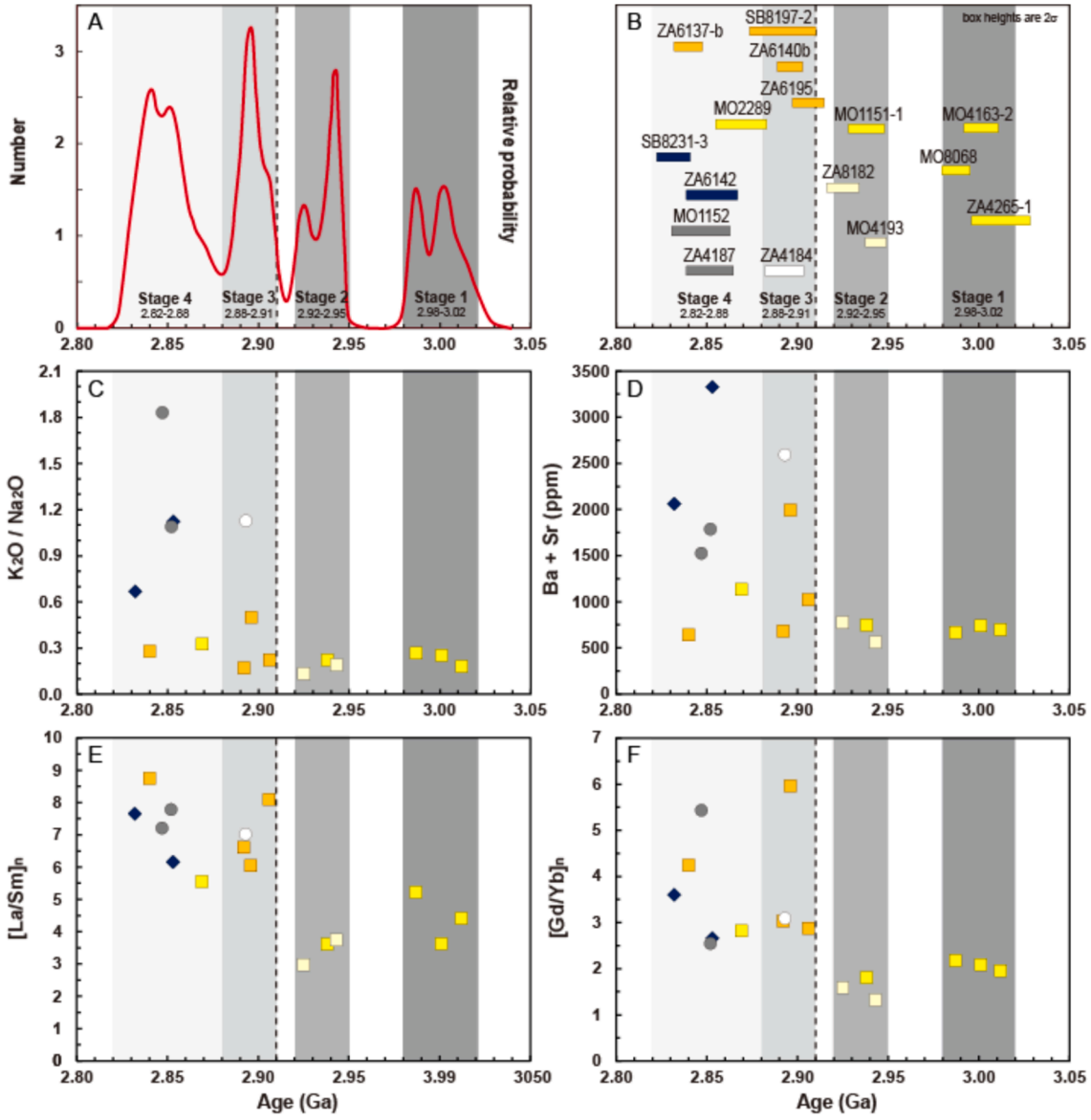

Fig. 11. A. Relative probability plot suggesting four major periods of magmatism. **B.** Age distribution diagram with their relative errors according to the different magmatic events that could be highlighted in A. **C.** K_2O/Na_2O vs. Age; **D.** Ba + Sr vs. Age; **E.** $[La/Sm]_n$ vs. Age; **F.** $[Gd/Yb]_n$ vs. Age.

6.2. Geochronology of plutonic rocks

The results of the geochronological study of granitoids rocks from the Chaillu massif are summarised in Fig. 11**A**. The relative probability diagram of all ages indicates four intervals of magmatic emplacement and, combined with the geochemical classification of the rocks, documents progressive change of magma composition with time (Fig. 11**B, C**).

Stage 1 from 3.02-2.98 Ga (±40 my) is recorded only in medium La/Yb tonalitic to trondhjemitic grey orthogneisses. Stage 2 from 2.96-2.92 Ga (±40 my) consists of different types of tonalitic to trondhjemitic grey gneisses joining the medium La/Yb TTG's of stage 1. High to low La/Yb ratios indicate source regions with or without residual garnet. Stage 3 from 2.91-2.88 Ga (±30 my) is characterized by the emplacement of tonalitic to trondhjemitic gneisses with high La/Yb ratios and potassic granites. High La/Yb ratios indicate source regions with residual garnet, and potassic granites melting of crustal component. Stage 4 from 2.88-2.82 Ga (±60 my) is marked by great diversification of magma comprising TTG, potassic granite, and sanukitoid. Three samples of this event comprise zircons with inherited ages indicating crustal recycling during this stage. In sample ZA8182, a low La/Yb TTG, inherited zircons dated at 2.99 and 3.10 Ga. These inherited ages may come from hydrated metasasites having melted and produced TTG melts. These metasasites could be linked to mantle upwelling (overturn upwelling zone, OUZO) at this time. Stages 3 and 4 demonstrate that the late Archean transition, characterized by coexisting TTGs, sanukitoids, and potassic granites, took place during a period of less than 100 my, between 2.91 and 2.82 Ga.

The first two stages, before 2.92 Ga, are characterized by low and medium La/Yb TTG granitoids. They have low K_2O/Na_2O ratios, low Ba and Sr contents, fractionated light rare earths ($[La/Sm]_n < 5.5$), and poorly fractionated heavy rare earths ($[Gd/Yb]_n < 2.5$; Fig. 11**C-F**). These TTGs were generated intermittently between 3.02 and 2.98 Ga, then between 2.95 and 2.92 Ga. The last two stages, after 2.91 Ga, are characterized by the coexistence of TTGs, sanukitoids and potassic granites. All these granitoids are characterized by strong fractionation of LREE ($[La/Sm]_n > 5.5$), and HREE ($[Gd/Yb]_n > 2.5$; Fig. 11**C-F**). Sanukitoids and potassic granites have high K_2O/Na_2O ratios, and high Ba and Sr contents (Fig. 11**C-F**). TTGs contemporary with sanukitoids and potassic granites have slightly higher K_2O/Na_2O ratios and Ba and Sr contents than TTGs older than 2.92 Ga.

6.3. Comparison with other Mesoarchean granitoids worldwide

Extensive Mesoarchean granitoids worldwide younger than 3.0 Ga can be subdivided into four groups: i) sodic granitoids (TTG); high-Mg granitoids (sanukitoids); iii) high-K granitoids (biotite- and two-micas granites); and iv) hybrid granitoids derived from interaction, between magmas or sources, of the three other groups (Smithies and Champion, 2000; Moyen et al., 2003; Whalen et al., 2004; Heilimo et al., 2011; Almeida et al., 2013; Laurent et al., 2014; Jiang et al., 2016; Santos and Oliveira, 2016; Jayananda et al., 2018; Singh et al., 2019). The dominant magma types are TTG suites, which consist of plagioclase-rich plutonic rocks (tonalites, trondhjemites, and granodiorites) with a sodic composition ($K_2O/Na_2O < 1$). They result from partial melting of enriched hydrous mafic rocks under high pressures in the stability field of garnet (Halla et al., 2009; Moyen, 2011; Moyen and Martin, 2012; Martin et al., 2014). Sanukitoids are generally late to post-tectonic, calc-alkaline to alkali-calcic, and metaluminous in character. In contrast to other late Archean granitoids; they vary widely in SiO_2, K_2O, K_2O/Na_2O ratios and are enriched in ferromagnesian oxides and CaO (Laurent et al., 2014). Syn- to post-tectonic high-K granitoids include peraluminous biotite- and two-mica granites marked by high SiO_2 and K_2O and low ferromagnesian oxides (Laurent et al., 2014).

Evolution from early TTG to late sanukitoid and high-K granitoid has been recognized in several cratons but is diachronous (Almeida et al., 2013; Romano et al., 2013; Laurent et al., 2014; Farina et al., 2015; Joshi et al., 2017; Singh et al., 2019). It ranges from 2.95 to 2.85 Ga in the Pilbara, Amazonian, São Francisco, and Ukrainian cratons, from 2.75 to 2.62 Ga in the Karelian, Kaapvaal, Superior, and Slave cratons (Smithies and Champion, 2000; Bibikova et al., 2008; Oliveira et al., 2009; Heilimo et al., 2011; Laurent et al., 2014; Teixeira et al., 2017), and from 2.60 to 2.50 Ga in the Dharwar and North China cratons (Laurent et al., 2014). At global scale, the Chaillu Inlier can be thus correlated with the Pilbara, Ukrainian, and especially the Amazonian and São Francisco cratons with which it shares many similarities.

The Congo Craton is generally correlated with the Sao Francisco craton due to: (1) the direct connection between the cratons when the South Atlantic Ocean is closed, and (2) the similarities between their Archean and Paleoproterozoic geodynamic evolutions. Several Archean blocks have been identified in the northern and southern parts of the Sao Francisco craton. In the northern part of the Sao Francisco craton, these are the Gavião, Guanambi-Correntina, Sobradinho, Jequié, Itabuna-Salvador-Curaçá and Serrinha blocks (Teixeira et al., 2017).

The Serrinha block shares common geological features with the Ntem-Chaillu block, based on the compilation of geological data, geochronology and metamorphic events. The main tectonic units of the Serrinha block are: (1) the Uauá block composed of grey gneisses of TTG affinity and age between ~ 3.20–3.10 Ga (Oliveira et al., 2010, 2011), ~2.95–2.90 Ga high-K and Mg granitoids of sanukitoid affinity (Oliveira and Amaral, 2014), 2.83–2.82 Ga high-pressure mafic granulites (Oliveira et al., 2019); and (2) the Retirolandia-Jacurici complexes, composed of migmatites and gray gneisses of TTG affinity, and ages between 3.10 and 2.90 Ga (Oliveira et al., 2010; Baldim and Oliveira, 2016), which host several mafic–ultramafic complexes).

In the Serrinha block, two distinct periods of magmatism may be identified: i) a first event older than 2.95 Ga produced only TTGs; and ii) a second magmatic event combines sanukitoids, potassic granites, and TTGs between 2.95 and 2.85 Ga. These two distinct periods of magmatism, with the same temporality, have been observed in the Amazonian craton. The Amazonian Craton has been subdivided into several provinces with distinct geochronology, structural patterns, and geodynamic settings. In the Carajàs Province, the Rio Maria Domain (RMD) is the oldest tectonic domain and consists of five major rock formations: i) greenstone belts (3.00–2.90 Ga; Macambira and Lancelot, 1996; Souza et al., 2001); ii) older TTGs (2.96–2.92 Ga; Almeida et al., 2011); iii) sanukitoids (2.87 Ga; Oliveira et al., 2009); iv) younger TTGs (2.86 Ga; Leite et al., 2004); and v) high-K calc-alkaline leucogranites (2.87–2.86 Ga; Althoff et al., 2000; Almeida et al., 2010, 2013). As in the Chaillu Inlier, two distinct periods of intermediate to felsic magmatism have been identified: i) the first event from 2.96 to 2.92 Ga produced TTGs with variable La/Yb and Sr/Y ratios similar to the ones in the Chaillu Inlier, and ii) the second magmatic event combines sanukitoids, potassic granites, and medium to high La/Yb TTGs younger than 2.88 Ga. According to Silva et al., (2018,2022), this magmatism corresponds to two geodynamic settings. The early stage from 2.96-2.92 Ga is associated with low-angle subduction, slab-derived melts and pronounced metasomatism of the mantle wedge. The late stage from 2.88-2.86 Ga took place in a transpressive collisional setting resulting in the production of mantle- and crust-derived magmas.

The 2.95–2.85 Ga period is marked in several cratons by the coexistence of medium to high La/Yb TTGs, with sanukitoids and potassic granites (Bleeker, 2003; Moyen et al., 2003; Jayananda et al., 2006; Laurent et al., 2014; Farina et al., 2015; Dall'Agnol et al., 2017) and has been interpreted as evidence for the onset of 'modern style' plate tectonics (Laurent et al., 2014). The particular petrogenesis of sanukitoids requires the interaction of supracrustal material (basalts, sediments) with mantle peridotite (Laurent et al., 2014). This implies the burial of supracrustal material by subduction-like processes. Due to higher Archean mantle temperatures (Herzberg et al., 2010), subduction was possibly intermittent and marked by the frequent rupture and dripping of basaltic materials into the mantle (Sizova et al., 2010; Moyen and van Hunen, 2012; Fischer and Gerya, 2016). According to Ge et al.,

(2018,2022), these intermittent subductions, interrupted by slab breakoff, allow water to be transported to the mantle depths. These hydrated magmas would be underplated or intruded into the overlying oceanic plate, and would enable the production of LP and MP TTGs at their base. Slab breakoff also seems to be the phenomenon that best explains the formation of sanukitoids (Whalen et al., 2004; Halla et al., 2009; Almeida et al., 2011; Mikkola et al., 2011). However frequent slab breakoff means that slab pull cannot be efficient and considered as the main driving force for the Archean tectonics (Bédard, 2018; Sizova et al., 2015). To explain Archean tectonics, Bédard et al. (2013) combined vertical thickening and lateral accretion into a model where global-scale mantle overturn events induce large-scale convective currents in the mantle. These currents push on the deep mantle keel of the craton and drive horizontal cratonic motion. This horizontal motion may induce convergent margins characterized by terrane accretion, tectonic imbrication, ('subcretion'), and anatexis of unsubductable oceanic lithosphere.

6.4. Mesoarchean history of the Chaillu inlier

In the northwestern Congo Craton, two distinct processes have been suggested to generated the TTG magmatism: i) a subduction setting (Tchameni et al., 2000; Pouclet et al., 2007; Shang et al., 2010; Akame et al., 2020); or ii) rising mantle plumes inducing partial melting of basaltic protoliths (Gatsé Ebotehouna et al., 2021; Li et al., 2016).

The 3.00–2.91 Ga TTGs represent an important event of felsic crust formation, characterized by medium La/Yb TTGs from 3.00 to 2.97 Ga, and by low and high La/Yb TTGs from 2.95 to 2.91 Ga. This implies that a short period of time (~90 my) elapsed to transform mafic crust into TTG-dominated felsic crust. During this period, TTGs evolved from medium to high La/Yb TTGs. This suggests an increasing melting depths from 30-45 km at 3.00–2.97 Ga to 45–60 km at 2.95–2.91 Ga (see section 6.1.1). TTGs may have been formed in progressive response to gradual thickening of a mafic crust.

Two geodynamic settings have been proposed for the subsequent TTG magmatism: i) an "igneous" model with rising mantle plumes causing partial melting of the basaltic protoliths (Bédard, 2006, 2018; Gatsé Ebotehouna et al., 2021; Li et al., 2016; Smithies et al., 2009; van Kranendonk et al., 2015) or ii) a "tectonic" model in a subduction environment (Akame et al., 2020; Pouclet et al., 2007; Shang et al., 2010; Tchameni et al., 2000) where vertical stacking of mafic crust causes melting at its base (Hiess et al., 2009; Sizova et al., 2010; Nutman et al., 2015). Whatever the model, when the crust exceeds 45 km in thickness, its base becomes gravitationally unstable due to its increased density relative to the underlying mantle (Johnson et al., 2013). This instability leads to the detachment of the lower crust, which in turn leads to the deep melting of basic materials and the production of high-La/Yb TTGs (Bédard, 2006; Zegers and van Keken, 2001). Crustal delamination may also explain local shallow melting contributed to low La/Yb TTGs. This hypothesis of crustal delamination implies that the lower crust has a basaltic composition. However, the base of the thick oceanic crust is essentially composed of anhydrous ultramafic and mafic cumulates, and such anhydrous compositions are unlikely to melt by dehydration to produce TTGs (Arndt, 2013, 2023; Roman and Arndt, 2020). Ge et al. (2023) found that Archean granitoids have magmatic fO_2, H_2O contents and H_2O/Ce ratios that correlate positively with depth of magma formation, implying the addition of large quantities of H_2O to the lower crust and mantle.

In summary, the new data confirm that Mesoarchean felsic crustal growth in the Chaillu inlier occurred in two main periods (Fig. 12). Prior 2.92 Ga, melting at depths of 30–45 km generated low to medium pressure TTGs. Mantle upwelling, or the overturn of an upwelling zone is considered as the driving force behind the anatexis of lower to middle mafic crust. After 2.91 Ga, the emplacement of large volumes of TTG, sanukitoid, and potassic granite documents the interaction of mantle peridotite with felsic melts and/or paragneiss. Tectonic imbrication

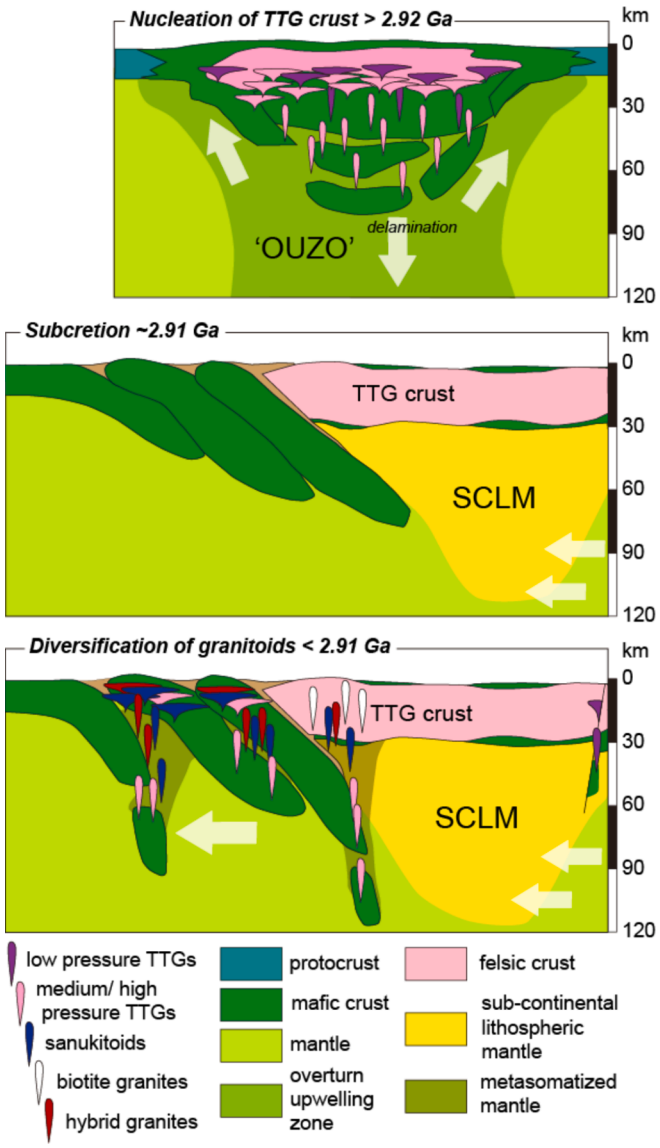

Fig. 12. Geodynamic model (modified from Laurent et al., 2019). stage 1: Between 3.00 and 2.91 Ga, the melting at shallow to deep depths induce the formation of low to high pressure TTGs. These repeated melting are certainly related to a mantle upwelling, an overturn upwelling zone. Stage 2: around 2.91 Ga, horizontal motion may induce convergent margins characterized by terrane accretion, tectonic imbrication or 'subcretion' of unsubductable oceanic lithosphere, this passive tectonic imbrication (subcretion) of proto-cratons could be due to the pressure created by mantle convection currents on their lithospheric keels. Stage 3: finally, this subcretion ends with the generation in a short time, between 2.89 and 2.83 Ga, of large volumes of diversified magmas (TTG, sanukitoid, and potassic granite) indicate interactions of peridotitic mantle with felsic melts and/or sediments, and fusion of crustal material. (Bédard et al., 2013).

(subcretion) of proto-cratons could be caused by mantle convection along their lithospheric keels (Bédard et al., 2013).

7. Conclusions

New geological mapping data of this study define four suites of Mesoarchean plutonic rocks: (i) tonalitic to trondhjemitic grey gneisses (TTG); (ii) mesocratic to melanocratic gneisses (sanukitoids s.l.); (iii) potassic granites; and (iv) pink-grey hybrid granitoids. The TTGs have been subdivided in low, medium, and high La/Yb rocks implying their origin from varying mantle depth. The mesocratic and melanocratic

gneisses are subdivided into sanukitoids and hybrid granitoids with sanukitoid affinity. Both groups are alkali-calcic to calc-alkaline, but they can be distinguished on their FeO^t/MgO ratios, Al_2O_3, K_2O, and some trace elements (Sr, Ba, Rb). The potassic granites are generated by partial melting of older felsic crust, essentially TTGs. The pink-grey granitoids are hybrid granitoids generated by the interaction between the magmas of TTGs and potassic granites.

These Mesoarchean plutonic suites record a temporal evolution with a tectono-magmatic two-stage model: i) a first stage (3.00–2.89 Ga) with TTG magmatism related to crustal delamination; and ii) a second stage with coexisting TTGs, sanukitoids, and biotite granites generated in a convergent setting with tectonic imbrication (or subcretion?), metasomatism of peridotitic mantle and anatexis of lithosphere. Similar evolution has been observed on other Archean cratonic domains worldwide, between 3.0 and 2.5 Ga.

CRediT authorship contribution statement

O. Blein: Writing – review & editing, Writing – original draft, Data curation, Conceptualization. **T. Fullgraf:** Writing – review & editing, Conceptualization. **M. Padel:** Writing – review & editing, Investigation, Conceptualization. **J. Melleton:** Writing – review & editing, Conceptualization. **M. Chevillard:** Writing – review & editing. **E. Gloaguen:** Writing – review & editing. **F. Boudzoumou:** Writing – review & editing. **F. Cagnard:** Writing – review & editing. **B. Le Bayon:** Writing – original draft. **L.-M. Djama:** . **Y. Callec:** Writing – review & editing, Project administration, Funding acquisition.

Declaration of competing interest

The authors declare that they have no known competing financial interests or personal relationships that could have appeared to influence the work reported in this paper.

Data availability

Data will be made available on request.

Acknowledgements

Support for this work was provided by the project “Appui au programme de cartographie géologique, d’inventaire minier du Congo, d’éducation et de formation professionnelle” (Asperbras Congo/BRGM project. 2013-2016). We thank Chris Hawkesworth and Rongfeng Ge for their reviews, valuable comments and suggestions.

Appendix A. Supplementary data

Supplementary data to this article can be found online at https://doi.org/10.1016/j.precamres.2024.107435.

References

Akame, J.M., Oliveira, E.P., Poujol, M., Hublet, G., Debaille, V., 2020. LA-ICP-MS zircon U-Pb dating, Lu-Hf, Sm-Nd geochronology and tectonic setting of the Mesoarchean mafic and felsic magmatic rocks in the Sangmelima granite-greenstone terrane, Ntem Complex (South Cameroon). Lithos 372–323, 1–22. https://doi.org/10.1016/j.lithos.2020.105702.

Almeev, R.R., Bolte, T., Nash, B.P., Holtz, F., Erdmann, M., Cathey, H.E., 2013. High temperature, low-H2O Silicic Magmas of the Yellowstone Hotspot: an Experimental Study of Rhyolite from the Bruneau-Jarbidge Eruptive Center, Central Snake River Plain. USA. J. Petrol. 53 (9), 1837–1866.

Almeida, J.A.C., Dall’Agnol, R., Dias, S.B., Althoff, F.J., 2010. Origin of the Archean leucogranodiorite-granite suites: evidence from the Rio Maria. Lithos 120, 23–257. https://doi.org/10.1016/j.lithos.2010.07.026.

Almeida, J.A.C., Dall’Agnol, R., Oliveira, M.A., Macambira, M.J.B., Pimentel, M.M., Ramo, O.T., Guimaraes, F.V., Leite, A.A.S., 2011. Zircon geochronology, geochemistry and origin of the TTG suites of the Rio Maria granite–greenstone terrane: implications for the growth of the Archean crust of the Carajas Province. Brazil. Precambr. Res. 187, 201–221. https://doi.org/10.1016/j.precamres.2011.03.004.

Almeida, J.A.C., Dall’Agnol, R., Leite, A.A.S., 2013. Geochemistry and zircon geochronology of the archean granite suites of the Rio Maria granite–greenstone terrane, Carajas Province. Brazil. J. s. Am. Earth Sci. 42, 103–126. https://doi.org/10.1016/j.jsames.2012.10.008.

Alonso-Perez, R., Muntener, O., Ulmer, P., 2009. Igneous garnet and amphibole fractionation in the roots of island arcs: experimental constraints on andesitic liquids. Contrib. Miner. Petrol. 157, 541–558.

Althoff, F.J., Barbey, P., Boullier, A.M., 2000. 2.8-3.0 Ga plutonism and deformation in the SE Amazonian craton: the Archean granitoids of Marajoara (Carajás Mineral province, Brazil). Precambr. Res. 104, 187–206. https://doi.org/10.1016/S0301-9268(00)00103-0.

Arndt, N.T., 2013. The formation and evolution of the continental crust. Geochemical Perspectives 3 (2), 405–533.

Barker, F., 1979. Trondhjemite: definition, environment and hypotheses of origin, in: F. Barker (Ed.), Trondhjemites, dacites and related rocks. Developments in Petrology, Amsterdam, 6, 1–11.

Baldim, M.R., Oliveira, E.P., 2016. Anatomy of the Alto Alegre gneiss dome, São Francisco Craton, Brazil: a geological record of transpression along a Palaeoproterozoic arc-continent collision zone. Precambr. Res. 286, 250–268. https://doi.org/10.1016/j.precamres.2016.10.004.

Beard, J.S., Lofgren, G.E., 1991. Dehydration melting andwater-saturated melting of basaltic and andesitic greenstones and amphibolites at 1, 3 and 6.9 kbar. J. Petrol. 32 (2), 365–401.

Bédard, J., 2006. A catalytic delamination-driven model for coupled genesis of Archaean crust and sub-continental lithospheric mantle. Geochim. Cosmochim. Ac. 70, 1188–1214. https://doi.org/10.1016/j.gca.2005.11.008.

Bédard, J.H., 2018. Stagnant lids and mantle overturns: implications for Archaean tectonics, magma genesis, crustal growth, mantle evolution, and the start of plate tectonics. Geosci. Front. 9, 19–49. https://doi.org/10.1016/j.gsf.2017.01.005.

Bédard, J.H., Harris, L.B., Thurston, P., 2013. The hunting of the snArc. Precambr. Res. 229, 20–48. https://doi.org/10.1016/j.precamres.2012.04.001.

Bibikova, E.V., Lobach-Zhuchenko, S.B., Artemenko, G.B., Claesson, S., Kovalenko, A.V., Krylov, I.N., 2008. Late Archean magmatic complexes of the Azov Terrane, Ukrainian Shield: geological setting, isotopic age, and sources of material. Petrology 16 (3), 211–231.

Blatter, D.L., Sisson, T.W., Hankins, W.B., 2013. Crystallization of oxidized, moderately hydrous arc basalt at mid- to lower-crustal pressures: implications for andesite genesis. Contrib. Mineral. Petr. 166 (3), 861–886.

Bleeker, W., 2003. The late Archean record: a puzzle in ca. 35 pieces. Lithos 71, 99–134. https://doi.org/10.1016/j.lithos.2003.07.003.

Bogaerts, M., Scaillet, B., Vander Auwera, J., 2006. Phase equilibria of the Lyngdal granodiorite (Norway): implications for the origin of metaluminous ferroan granitoids. J. Petrol. 47 (12), 2405–2431.

Bouton, P., Thiéblemont, D., Gouin, J., Cocherie, A., Guerrot, C., Tegyey, M., Préat, A., Simo Ndounze, S., Kassadou, A.B., Boulingui, B., Ekogha, H., Moussavou, M., 2009. Notice explicative de la Carte géologique de la République du Gabon à 1/200 000, feuille Franceville – Boumango. Editions DGMG – Ministère des Mines, du Pétrole, des Hydrocarbures. Libreville, Gabon.

Caen-Vachette, M., Vialette, Y., Bassot, J.P., Vidal, P., 1988. Apport de la géochronologie isotopique à la connaissance de la géologie gabonaise. Chronique De La Recherche Minière, BRGM, Orléans 491, 35–54.

Champion, D.C., Sheraton, J.W., 1997. Geochemistry and Nd isotope systematics of Archaean granites of the Eastern Goldfields, Yilgarn Craton, Australia: implications for crustal growth processes. Precambr. Res. 83, 109–132. https://doi.org/10.1016/S0301-9268(97)00007-7.

Chevalier, L., Makanga, J.F., Thomas, R.J., 2002. Notice explicative de la carte géologique de la République Gabonaise à 1/1.000.000. Editions DGMG Gabon, p. 195 p..

Chevillard, M., Fullgraf, T., Blein, O., Badinier, G., Boudzoumou, F., Joannes, C., Rouzeau, O., Callec, Y., 2017a. Carte géologique de la République du Congo à 1/200.000, Feuille Ewo. Editions BRGM.

Chevillard, M., Fullgraf, T., Blein, O., Bauer, H., Prognon, F., Badinier, G., Vic, G., Boudzoumou, F., Loumbi Tatinéné, C.M., Ngandziami, P.V., Doumat-Sangoyi, A.J., Moutsamboté Sounda, U.G., Callec, Y., 2017b. Carte géologique de la République du Congo à 1/200.000, Feuille Mbomo. Editions BRGM.

Chevillard, M., Callec, Y., Gloaguen, E., Paquet, F., Serrano, O., Fullgraf, T., Blein, O., Boudzoumou, F., Joannes, C., Devoir, A., Guembo Massala, H.M.B., Souati Mibansa, D.G., 2017c. Carte géologique de la République du Congo à 1/200.000, Feuille Mossendjo. Editions BRGM.

Dall’Agnol, R., da Cunha, I.R.V., Guimaraes, F.V., de Oliveira, D.C., Teixeira, M.F.B., Feio, G.R.L., Lamarao, C.N., 2017. Mineralogy, geochemistry, and petrology of Neoarchean ferroan to magnesian granites of Carajas Province, Amazonian Craton: the origin of hydrated granites associated with charnockites. Lithos 277, 3–32. https://doi.org/10.1016/j.lithos.2016.09.032.

Dey, S., Nandy, J., Choudhary, A.K., Liu, Y., Zong, K., 2014. Origin and evolution of granitoids associated with the Kadiri greenstone belt, eastern Dharwar craton: a history of orogenic to anorogenic magmatism. Precambr. Res. 246, 64–90. https://doi.org/10.1016/j.precamres.2018.04.019.

Dey, S., Halla, J., Kurhila, M., Nandy, J., Heilimo, E., Pal, S., 2016. Geochronology of Neoarchaean granitoids of the NW eastern Dharwar craton: implications for crust formation. Geol. Soc. London Spec. Publ. 449 https://doi.org/10.1144/SP449.9. SP449–9.

Farina, F., Albert, C., Lana, C., 2015. The Neoarchean transition between medium-and high-K granitoids: clues from the Southern Sao Francisco Craton Brazil. Precambr. Res. 266, 375–394. https://doi.org/10.1016/j.precamres.2015.05.038.
Faure, G., Mensing, T.M., 2005. Isotopes: principles and applications. Wiley, Hoboken, p. 897.
Fischer, R., Gerya, T., 2016. Regimes of subduction and lithospheric dynamics in the Precambrian: 3D thermomechanical modelling. Gondwana Res. 37, 53–70. https://doi.org/10.1016/j.gr.2016.06.002.
Frost, B.R., Barnes, C.G., Collins, W.J., Arculus, R.J., Ellis, D.J., Frost, C.D., 2001. A geochemical classification for granitic rocks. Journal of Petrology 42, 2033–2048. https://doi.org/10.1093/petrology/42.11.2033.
Fullgraf, T., Chevillard, M., Le Bayon, B., Boudzoumou, F., Joannes, C., Blein, O., 2017). Carte géologique de la République du Congo à 1/200.000, Feuille Mékambo-Mintom. Editions BRGM.
Gatsé Ebotehouna, C., Xie, Y., Adomako-Ansah, K., Qu, Y., 2021. Petrology, geochemistry, and zircon U-Pb-Lu–Hf isotopes of granitoids from the Ivindo basement complex of the Souanké area, Republic of Congo: insights into the evolution of Archean continental crust. Geol. J. 56, 4861–4887. https://doi.org/10.1002/gj.4219.
Ge, R., Zhu, W., Wilde, S.A., Wu, H., 2018. Remnants of Eoarchean continental crust derived frm a subducted proto-arc. Science Advances 4 (2), aao3159.
Ge, R., Wilde, S.A., Zhu, W., Zhou, T., Si, Y., 2022. Formation and evolution of Archean continental crust: a thermodynamic – geochemical perspective of granitoids from the Tarim Craton. NW Chine. Earth-Science Reviews 234, 104219. https://doi.org/10.1016/j.earscirev.2022.104219.
Ge, R., Wilde, S.A., Zhu, W., Wang, X., 2023. Earth's early continental crust formed from wet and oxidizing arc magmas. Nature 623, 334–339. https://doi.org/10.1038/s41586-023-06552-0.
Gloaguen, E., Callec, Y., Chevillard, M., Fullgraf, T., Issautier, B., Badinier, G., Boudzoumou, F., Préat, A., Thiéblemont, D., Joannes, C., Le Métour, J., Damba, F., Biboussi, J., 2017a. Carte géologique de la République du Congo à 1/200.000, Feuille Sibiti. Editions BRGM.
Gloaguen, E., Chevillard, M., Fullgraf, T., Blein, O., Boudzoumou, F., Joannes, C., Badinier, G., Issautier, B., Callec, Y., Madous, P.L., Mboussa, D.J.W., Tsossolo Moundele, G., Bounsana, R.B., 2017b. Carte géologique de la République du Congo à 1/200.000, Feuille Zanaga. Editions BRGM.
Halla, J., 2005. Late Archean high-Mg granitoids (sanukitoids) in the southern Karelian domain, eastern Finland: Pb and Nd isotopic constraints on crust–mantle interactions. Lithos 79 (1–2), 161–178. https://doi.org/10.1016/j.lithos.2004.05.007.
Halla, J., van Hunen, J., Heilimo, E., Holtta, P., 2009. Geochemical and numerical constraints on Neoarchaean plate tectonics. Precambr. Res. 174, 155–162. https://doi.org/10.1016/j.precamres.2009.07.008.
Heilimo, E., Halla, J., Holtta, P., 2010. Discrimination and origin of the sanukitoid series: geochemical constraints from the Neoarchean western Karelian Province Finland. Lithos 115, 27–39. https://doi.org/10.1016/j.lithos.2009.11.001.
Heilimo, E., Halla, J., Huhma, H., 2011. Single-grain zircon U-Pb age constraints of the western and eastern sanukitoid zones in the Finnish part of the Karelian Province. Lithos 121, 87–99. https://doi.org/10.1016/j.lithos.2010.10.006.
Herzberg, C., Condie, K.C., Korenaga, J., 2010. Thermal history of the earth and its petrological expression. Earth Planet. Sci. Lett. 292, 79–88. https://doi.org/10.1016/j.epsl.2010.01.022.
Hiess, J., Bennett, V.C., Nutman, A.P., Williams, I.S., 2009. In situ U-Pb, O and Hf isotopic compositions of zircon and olivine from Eoarchaean rocks, West Greenland: New insights to making old crust. Geochim. Cosmochim. Acta 73, 4489–4516. https://doi.org/10.1016/j.gca.2009.04.019.
Issautier, B., Chevillard, M., Fullgraf, T., Callec, Y., Le Bayon, B., Schroetter, J.-M., Gloaguen, E., Blein, O., Prognon, F., Badinier, G., Vic, G., Bruyère, D., Boudzoumou, F., Delpomdor, F., 2017. Carte géologique de la République du Congo à 1/200.000, Feuille Sembé-Souanké. Editions BRGM.
Jayananda, M., Chardon, D., Peucat, J.-J., Capdevila, R., 2006. 2.61 Ga potassic granites and crustal reworking in the western Dharwar craton, southern India: tectonic, geochronologic and geochemical constraints. Precambr. Res. 150, 1–26. https://doi.org/10.1016/j.precamres.2006.05.004.
Jayananda, M., Santosh, M., Aadhiseshan, K.R., 2018. Formation of Archean 3600–2500 Ma continental crust in the Dharwar Craton, southern India. Earth Sci. Rev. 181, 12–42. https://doi.org/10.1016/j.earscirev.2018.03.013.
Jiang, N., Guo, J., Fan, W., Hu, J., Zong, K., Zhang, S., 2016. Archean TTGs and sanukitoids from the Jiaobei terrain, North China craton: insights into crustal growth and mantle metasomatism. Precambr. Res. 281, 656–672. https://doi.org/10.1016/j.precamres.2016.06.019.
Johnson, T.E., Brown, M., Kaus, B.J., Vantongeren, J.A., 2013. Delamination and recycling of Archaean crust caused by gravitational instabilities. Nat. Geosci. 7, 47–52.
Joshi, K.B., Bhattacharjee, J., Rai, G., Halla, J., Ahmad, T., Kurhila, M., Choudhary, A.K., 2017. The diversification of granitoids and plate tectonic implications at the Archaean-Proterozoic boundary in the Bundelkhand Craton, Central India. Geol. Soc. London Spec. Publ. 449, 123–157. https://doi.org/10.1144/SP449.8.
Keller, C.B., Schoene, B., 2012. Statistical geochemistry reveals disruption in secular lithospheric evolution about 2.5 Gyr ago. Nature 485, 490. https://doi.org/10.1038/nature11024.
Kessi, C., 1992. Le socle Archéen et les formations ferrifères du Chaillu au Congo. University of Rennes, Rennes, France. Doctorat Thesis.
Laurent, O., Martin, H., Doucelance, R., Moyen, J.F., Paquette, J.L., 2011. Geochemistry and petrogenesis of high-K "sanukitoids" from the Bulai pluton, Central Limpopo Belt, South Africa: implications for geodynamic changes at the Archaean-Proterozoic boundary. Lithos 123, 73–91. https://doi.org/10.1016/j.lithos.2010.12.009.
Laurent, O., Martin, H., Moyen, J.F., Doucelance, R., 2014. The diversity and evolution of late-Archean granitoids: evidence for the onset of "modern-style" plate tectonics between 3.0 and 2.5 Ga. Lithos 205, 208–235. https://doi.org/10.1016/j.lithos.2014.06.012.
Laurent, O., Couzinié, S., Zeh, A., Vanderhaeghe, O., Moyen, J.F., Villaros, A., Gardien, V., Chelle-Michou, C., 2017. Protracted, coeval crust and mantle melting during Variscan late-orogenic evolution: U-Pb dating in the eastern French Massif Central. Int. J. Earth Sci. 106 (2), 421–451.
Laurent, O., Martin, H., Moyen, J.F., Doucelance, R., 2019. Building up the first continents: Mesoarchean to Paleoproterozoic crustal evolution in West Troms, Norway, inferred from granitoids petrology, geochemistry and Ziron U-Pb/Lu-Hf isotopes. Precambr. Res. 205, 208–235. https://doi.org/10.1016/j.precamres.2019.12.020.
Leite, A.A.S., Dall'Agnol, R., Macambira, M.J.B., Althoff, F.J., 2004. Geologia e geocronologia dos granitóides arqueanos da região de Xinguara (PA) e suas implicações na evolução do terreno granito-greenstone de Rio Maria. Revista Brasileira De Geociências 34, 447–458.
Li, X.-H., Chen, Y., Li, J., Yang, C., Ling, X.-X., Tchouankoue, J.P., 2016. New isotopic constraints on age and origin of Mesoarchean charnockite, trondhjemite and amphibolite in the Ntem Complex of NW Congo Craton, southern Cameroon. Precambr. Res. 276, 14–23. https://doi.org/10.1016/j.precamres.2016.01.027.
Loemba, A.P.R., Ferreira, A., Plavy Ntsiele, L.J.E., Opo, U.F., Bazebizonza Tchiguina, N. C., Nkodia, H.-M.-D.-V., Klausen, M., 2023. Archean crustal generation and Neoproterozoic partial melting in the Ivindo basement, NW Congo craton, Republic of Congo: Petrology, geochemistry and zircon U-Pb geochronology constraints. Journal of African Earth Sciences 200, 104852. https://doi.org/10.1016/j.jafrearsci.2023.104852.
Ludwig, K.R., 2003. Isoplot/Ex Version 3.00, A Geochronological Toolkit for Microsoft Excel: Berkeley Geochronology Center Special. Publication 4, 73 pp.
Macambira, M.J.B., Lancelot, J., 1996. Time constraints for the formation of the Archean Rio Maria Crust, Southeastern Amazonian Craton. Brazil. Int. Geol. Rev. 38, 1134–1142.
Martel, C., Pichavant, M., Holtz, F., Scaillet, B., Bourdier, J.L., Traineau, H., 1999. Effects of fO_2 and H_2O on andesite phase relations between 2 and 4 kbar. J. Geophys. Res. Solid Earth 104 (B12), 29453–29470.
Martin, H., Moyen, J.F., Rapp, R., 2009. The sanukitoid series: Magmatism at the Archaean-Proterozoic transition. Earth Environ. Sci. Trans. r. Soc. Edinburgh 100, 15–33. https://doi.org/10.1130/2010.2472(02).
Martin, H., Moyen, J.-F., Guitreau, M., Blichert-Toft, J., Le Pennec, J.-L., 2014. Why Archaean TTG cannot be generated by MORB melting in subduction zones. Lithos 198–199, 1–13. https://doi.org/10.1016/j.lithos.2014.02.017.
Martin, H., 1994. The Archaean grey gneisses and the genesis of continental crust, in: Condie, K.C. (Ed.), Archaean Crustal Evolution. Developments in Precambrian Geology, 11, pp. 205–260.
Mayaga-Mikolo, F., 1996. Chronologie des évènements sédimentaires, magmatiques et tectono-métamorphiques du Précambrien d'Afrique centrale occidentale (Gabon). Tectonogenèse Ogooué et héritage Archéen. In: Thèse De Doctorat D'université, Clermont-Ferrand-1 (185. Univ. Blaise-Pascal, p. p.)..
Meinhold, G., Morton, A.C., Fanning, C.M., Frei, D., Howard, J.P., Phillips, R.J., Strogen, D., Whitham, A.G., 2011. Evidence from detrital zircons for recycling of Mesoproterozoic and Neoproterozoic crust recorded in Paleozoic and Mesozoic sandstones of southern Libya. Earth Planet. Sci. Lett. 312, 164–175. https://doi.org/10.1016/j.epsl.2011.09.056.
Mikkola, P., Huhma, H., Heilimo, E., Whitehouse, M., 2011. Archean crustal evolution of the Suomussalmi district as part of the Kianta Complex, Karelia: constraints from geochemistry and isotopes of granitoids. Lithos 125, 287–307. https://doi.org/10.1016/j.lithos.2011.02.012.
Montel, J.M., Vielzeuf, D., 1997. Partial melting of metagreywackes, part II. Compositions of minerals and melts. Contrib. Miner. Petrol. 128, 176–196.
Moyen, J.F., 2011. The composite Archaean grey gneisses: petrological significance, and evidence for a non-unique tectonic setting for Archaean crustal growth. Lithos 123, 21–36. https://doi.org/10.1016/j.lithos.2010.09.015.
Moyen, J.F., Laurent, O., 2018. Archaean tectonic systems: a view from igneous rocks. Lithos 302–303, 99–125. https://doi.org/10.1016/j.lithos.2017.11.038.
Moyen, J.F., Martin, H., Jayananda, M., Auvray, B., 2003. Late Archaean granites: a typology based on the Dharwar Craton (India). Precambr. Res. 127, 103–123. https://doi.org/10.1130/G32729.1.
Moyen, J.F., Martin, H., 2012. Forty years of TTG research. Lithos 148, 312–336. https://doi.org/10.1016/j.lithos.2012.06.010.
Moyen, J.F., van Hunen, J., 2012. Short term episodicity of Archaean subduction. Geology 40 (5), 451–454. https://doi.org/10.1130/G322894.1.
Nagel, T.J., Hoffmann, J.E., Munker, C., 2012. Generation of Eoarchean tonalite-trondhjemite-granodiorite series from thickened mafic arc crust. Geology 40, 375–378. https://doi.org/10.1130/G32729.1.
Nédélec, A., Nsifa, E.N., Martin, H., 1990. Major and trace element geochemistry of the Archaean Ntem plutonic complex (South Cameroon): petrogenesis and crustal evolution. Precambr. Res. 47, 35–50. https://doi.org/10.1016/0301-9268(90)90029-P.
Nutman, A.P., Bennett, V.C., Friend, C.R.L., 2015. The emergence of the Eoarchaean proto-arc: evolution of a c. 3700 Ma convergent plate boundary at Isua, southern West Greenland. Geol. Soc. London 389, 113–133. https://doi.org/10.1144/SP389.5.

Oliveira, E.P., Amaral, W.S., 2014. Mesoarchaean modern-style plate tectonics in the Uauá terrane, Serrinha Block, Bahia: evidence from 3.0 Ga sanukitoids and high-pressure granulites. Anais do 47° Congresso Brasileiro de Geologia, Salvador, Bahia.
Oliveira, M.A., Dall'Agnol, R., Althoff, F.J., Leite, A.A.S., 2009. Mesoarchean sanukitoid rocks of the Rio Maria granite-greenstone terrane, Amazonian craton, Brazil. Journal of South American Earth Sciences 27, 146–160. https://doi.org/10.1016/j.jsames.2008.07.003.
Oliveira, E.P., McNaughton, N.J., Armstrong, R., 2010. Mesoarchaean to Palaeoproterozoic growth of the northern Segment of the Itabuna-Salvador-Curaçá orogen, São Francisco craton, Brazil. In: Kusky, T., Mingguo, Z., Xiao, Z. Eds., The Evolving Continents: Understanding Processes of Continental Growth. Geol. Soc. Lond. Spec. Publ. 338, 263–286. http://doi:10.1144/SP338.13.
Oliveira, E.P., Talavera, C., Windley, B.F., Zhao, L., Semprich, J.J., McNaughton, N.J., Amaral, S.W., Sombini, G., Navarro, M., Silva, D., 2019. Mesoarchaean (2820 Ma) high-pressure mafic granulite at Uauá, São Francisco Craton, Brazil, and its potential significance for the assembly of Archaean supercratons. Precambr. Res. 331 https://doi.org/10.1016/j.precamres.2019.105366.
Paquet, F., Callec, Y., Serrano, O., Chevillard, M., Fullgraf, T., Moungalla, J., Boumbouet, G., 2017. Carte géologique de la République du Congo à 1/200 000. Feuille Nyanga, Editions BRGM.
Patiño-Douce, A.E., Beard, J.S., 1996. Effects on P, *f*(O2) and Mg/Fe ratio on dehydration melting of model metagreywackes. J. Petrol. 37 (5), 999–1024.
Patiño-Douce, A.E., Harris, N., 1998. Experimental constraints on Himalayan anatexis. J. Petrol. 39 (4), 689–710.
Patiño-Douce, A.E., Johnston, D., 1991. Phase equilibria and melt productivity in the politic system: implications for the origin of peraluminous granitoids and aluminous granulites. Contrib. Miner. Petrol. 107, 202–218.
Pickering, J.M., Johnston, D.A., 1998. Fluid-absent melting behavior of a two-mica metapelite: experimental constraints on the origin of black hills granite. J. Petrol. 39 (10), 1787–1804.
Pouclet, A., Tchameni, R., Mezger, K., Vidal, M., Nsifa, E., Shang, C., Penaye, J., 2007. Archaean crustal accretion at the northern border of the Congo Craton (South Cameroon). The charnockite-TTG link. Bull. Soc. Geol. Fr. 178, 331–342. https://doi.org/10.2113/gssgfbull.178.5.331.
Prabhakar, B.C., Jayananda, M., Shareef, M., Kano, T., 2009. Syn-plutonic mafic injections into crystallizing granite pluton from Gurgunta area, northern part of eastern Dharwar Craton: implications for magma chamber processes. J. Geol. Soc. India 74, 171–188. https://doi.org/10.1007/s12594-009-0120-y.
Prian, J.-P., Johan, V., 1989. Contribution à la reconnaissance géologique et pétrographique de l'Archéen du massif du Chaillu et du Francevillien du bassin des Abeilles (région de Koulamoutou – Latoursville, Gabon). Rapport BRGM 89 GAB 079 GEO, texte 55 p., 4 pl. photos, 3 annexes.
Prian, J.P., Eko N'Dong, J., Coste, B., 1991. Synthèse géologique et géochimique, potentialités minières du degré carré Mouila (Archéen et Protérozoïque du Gabon central), avec carte géologique à 1/200 000. Synthèse du district aurifère d'Etéké, Edition BRGM, DGMG, Libreville, Gabon.
Rapp, R.P., Watson, E.B., 1995. Dehydration melting of metabasalt at 8–32 kbar: implications for continental growth and crust–mantle recycling. J. Petrol. 36 (4), 891–931.
Roman, A., Arndt, N.T., 2020. Differentiated Archean oceanic crust: its thermal structure, mechanical stability and a test of the sagduction hypothesis. Geochim. Cosmo. Acta. 278, 65–77. https://doi.org/10.1016/J.GCA.2019.07.009.
Romano, R., Lana, C., Alkmim, F.F., Stevens, G., Armstrong, R., 2013. Stabilization of the southern portion of the Sao Francisco craton, SE Brazil, through a long-lived period of potassic magmatism. Precambr. Res. 224, 143–159. https://doi.org/10.1016/j.precamres.2012.09.002.
Santos, M.N.S., Oliveira, D.C., 2016. Rio Maria granodiorite and associated rocks of Ourilandia do Norte-Carajas province: petrography, geochemistry and implications for sanukitoid petrogenesis. J. s. Am. Earth Sci. 72, 279–301. https://doi.org/10.1016/j.jsames.2016.09.002.
Shang, C.K., Liégeois, J.-P., Satir, M., Frisch, W., Nsifa, E.N., 2010. Late Archaean high-K granite geochronology of the northern metacratonic margin of the Archaean Congo craton, Southern Cameroon: evidence for Pb-loss due to non-metamorphic causes. Gondwana Res. 18, 337–355. https://doi.org/10.1016/j.gr.2010.02.008.
Shirey, S.B., Hanson, G.N., 1984. Mantle-derived Archaean monzodiorites and trachyandesites. Nature 310, 222–224. https://doi.org/10.1038/310222a0.
Silva, L.R., Oliveira, D.C., Santos, M.N.S., 2018. Diversity, origin and tectonic significance of the Mesoarchean granitoids of Ourilândia do Norte, Carajás province (Brazil). J. s. Am. Earth Sci. 82, 33–61. https://doi.org/10.1016/j.jsames.2017.12.004.
Silva, L.R., Oliveira, D.C., Nascimento, A.C., Lamarao, C.N., Almeida, J.A.C., 2022. The Mesoarchean plutonic complex from the Carajas province, Amaznian craton: Petrogenesis, zircon U-Pb SHRIMP geochronology and tectonic implications. Lithos 432–433, 106901. https://doi.org/10.1016/j. jlithos.2022.106901.
Singh, J., Johannes, W., 1996. Dehydration melting of tonalites. 2. Compositions of melts and solids. Contrib. Miner. Petrol. 125, 26–44.
Singh, P.K., Verma, S.K., Singh, V.K., Moreno, J.A., Oliveira, E.P., Mehta, P., 2019. Geochemistry and petrogenesis of sanukitoids and high-K anatectic granites from the Bundelkhand Craton, India: Implications for late Archean crustal evolution. Journal of African Earth Sciences 174, 263–282. https://doi.org/10.1016/j.jseaes.2018.12.013.
Sisson, T.W., Grove, T.L., 1993. Experimental investigations of the role of H2O in calc-alkaline differentiation and subduction zone magmatism. Contrib. Miner. Petrol. 113, 143–166.
Sisson, T.W., Ratajeski, K., Hankins, W.B., Glazner, A.F., 2005. Voluminous granitic magmas from common basaltic sources. Contrib. Miner. Petrol. 148, 635–661.
Sizova, E., Gerya, T., Brown, M., Perchuk, L.L., 2010. Subduction styles in the Precambrian: insight from numerical experiments. Lithos 116, 209–229. https://doi.org/10.1016/j.lithos.2009.05.028.
Sizova, E., Gerya, T., Stuwe, K., Brown, M., 2015. Generation of felsic crust in the Archean: a geodynamic modeling perspective. Precambr. Res. 271, 198–224. https://doi.org/10.1016/j.precamres.2015.10.005.
Skjerlie, K.P., Johnston, A.D., 1996. Vapour-absen tmelting from 10 to 20 kbar of crustal rocks that contain multiple hydrous phases: implications for anatexis in the deep to very deep continental crust and active continental margins. J. Petrol. 37, 661–691.
Sláma, J., Košler, J., Condon, D.J., Crowley, J.L., Gerdes, A., Hanchar, J.M., Horstwood, M.S.A., Morris, G.A., Nasdala, L., Norberg, N., Schaltegger, U., Schoene, B., Tubrett, M.N., Whitehouse, M.J., 2008. Plešovice zircon – a new natural reference material for U-Pb and Hf isotopic microanalysis. Chem. Geol. 249, 1–35. https://doi.org/10.1016/j.chemgeo.2007.11.005.
Smithies, R.H., Champion, D.C., 2000. The Archaean high-Mg diorite suite: links to tonalite-trondhjemite-granodiorite magmatism and implications for early Archaean crustal growth. Journal of Petrology 41, 1653–1671. https://doi.org/10.1093/petrology/41.12.1653.
Smithies, R.H., Champion, D.C., van Kranendonk, M.J., 2009. Formation of Paleoarchean continental crust through infracrustal melting of enriched basalt. Earth Planet. Sci. Lett. 281, 298–306. https://doi.org/10.1016/j.epsl.2009.03.003.
Souza, Z.S., Potrel, H., Lafon, J.M., Althoff, F.J., Pimentel, M.M., Dall'Agnol, R., Oliveira, C.G., 2001. Nd, Pb and Sr isotopes of the Identidade Belt, an Archaean greenstone belt of the Rio Maria region (Carajas Province, Brazil): Implications for the Archaean geodynamic evolution of the Amazonian Craton. Precamb. Res. 109, 293–315. https://doi.org/10.1016/S0301-9268(01)00164-4.
Stevens, G., 1995. Compositional controls on partial melting in high-grade metapelites; a petrological and experimental study. University of Manchester unpublished Ph.D. thesis.
Streckeisen, A., Le Maitre, R.W.L., 1979. A Chemical Approximation to Modal QAPF Classification of the Igneous Rocks: Neues Jahrbuch Fur Mineralogie Abhandlungen 136, 169–206.
Sun, S.S., McDonough, W.F., 1989. Chemical and isotopic systematics of oceanic basalts: implications for mantle composition and processes. In: Saunders, A.D., Norry, M.J. (Eds.), Magmatism in the Ocean Basins, 42. (Special publication). Geological Society, pp. 313–345.
Sylvester, P.J., 1994. Archaean granite plutons. In: Condie, K.C. (Ed.), Archaean Crustal Evolution. Developments in Precambrian Geology, vol. 11. Elsevier, Amsterdam, pp. 261–314.
Talavera, C., Montero, P., Martinez Poyatos, D., Williams, I.S., 2012. Ediacaran to Lower Ordovician age for rocks ascribed to the Schist-Graywacke Complex (Iberian Massif, Spain): evidence from detrital zircon SHRIMP U-Pb geochronology. Gondwana Res. 22, 928–942. https://doi.org/10.1016/j.gr.2012.03.008.
Tchameni, R., Mezger, K., Nsifa, N.E., Pouclet, A., 2000. Neoarchæan crustal evolution in the Congo Craton: evidence from K rich granitoids of the Ntem Complex, southern Cameroon. J. Afr. Earth Sci. 30, 133–147. https://doi.org/10.1016/S0899-5362(00)00012-9.
Teixeira, W., Oliveira, E.P., Marques, L.S., 2017. Nature and Evolution of the Archean Crust of the São Francisco Craton. In: Heilbron, M., Cordani, U.G., Alkmim, F.F. (Eds.), São Francisco Craton, Eastern Brazil Tectonic Genealogy of a Miniature Continent. Springer International Publishing, pp. 29–56. https://doi.org/10.1007/978-3-319-01715-0_3.
Thiéblemont, D., Castaing, M., Billa, M., Bouton, P., Préat, A., 2009. Notice explicative de la carte géologique et des ressources minérales de la République Gabonaise à 1/1.000.000. DGMG- Ministère Des Mines, Du Pétrole Et Des Hydrocarbures, Libreville.
Thiéblemont, D., Liégeois, J.-P. Fernandez-Alonso, M., Ouabadi, A., Le Gall, B., Maury, R., Vidal, M., Ouattara, G., Tchameni, R., Michard, A., Nehlig, P., Rossi, P., Chêne, F., 2017. Geological map of Africa at 1:10M scale, CGMW-BRGM 2016.
Thomas, R.J., Makanga, J.F., Chevallier, L., 2001. Notice explicative de la carte géologique de la République Gabonaise à 1/1.000.000, 2ème édition. Éditions DGMG, Gabon, pp. 195.
Toteu, S.F., Michard, A., Bertran, J.M., Rocci, G., 1987. U-Pb dating of Precambrian rocks from northern Cameroon, orogenic evolution and chronology of the Pan-African belt of central Africa. Precambr. Res. 37, 71–87. https://doi.org/10.1016/0301-9268(87)90040-4.
van Kranendonk, M.J., Smithes, R.H., Griffin, W.L., Huston, D.L., Hickman, A.H., Champion, D.C., Anhaeusser, C.R., Pirajno, F., 2015. Making it thick: a volcanic plateau origin of Palaeoarchean continental lithosphere of the Pilbara and Kaapvaal cratons. Geol. Soc. London 389, 83–111. https://doi.org/10.1144/SP389.12.
Vielzeuf, D., Holloway, J.R., 1988. Experimental determination of the fluid-absent melting relations in the pelitic system. Consequences for crustal differentiation. Contrib. Miner. Petrol. 98, 257–276.
Watkins, J.M., Clemens, J.D., Treloar, P.J., 2007. Archaean TTGs as sources of younger granitic magmas: melting of sodic metatonalites at 0.6–1.2 GPa. Contrib. Miner. Petrol. 154, 91–110.
Whalen, J.B., Percival, J.A., McNicoll, V.J., Longstaffe, F.J., 2004. Geochemical and isotopic (Nd–O) evidence bearing on the origin of late- to post-orogenic high-K granitoid rocks in the western superior province: implications for late-Archaean tectonomagmatic processes. Precambr. Res. 132, 303–326. https://doi.org/10.1016/j.precamres.2003.11.007.

Wolf, M.B., Wyllie, P.J., 1994. Dehydration-melting of amphibolite at 10 kbar: the effects of temperature and time. Contrib. Miner. Petrol. 115, 369–383.
Zamora, D., 2000. Fusion de la croûte océanique subductée: approche expérimentale et géochimique. Université Blaise-Pascal, Clermont-Ferrand, France, p. 314. Ph.D. thesis.
Zegers, T.E., van Keken, P.E., 2001. Middle Archean continent formation by crustal delamination. Geology 29 (12), 1083–1086. https://doi.org/10.1130/0091-7613(2001)029<1083:MACFBC>2.0.CO;2.